Enhancer-driven gene regulatory network of forebrain human development provides insights into autism

Short title: Gene regulatory network in human forebrain organoids

Alexandre Jourdon[1,2]†, Jessica Mariani[1,2]†, Abhiram Natu[1,2]†, Feinan Wu[1,2]†, Boxun Li[3,4], Davide Capauto[1,2], Kevin T. Hagy[3,4], Scott Norton[1], Livia Tomasini[1,2], Alexias Safi[4,5], Anahita Amiri[1], Jeremy Schreiner[1], Cindy Khanh Nguyen[1], Neal Nolan[1], Matthew P. Nelson[6], Daniel M. Ramos[6], Michael E. Ward[6,10], Anna Szekely[7,2], James C. McPartland[1], Kevin Pelphrey[1,8], Pamela Ventola[1], Katarzyna Chawarska[1], Charlie A Gersbach[3,4], Gregory E. Crawford[4,5], Alexej Abyzov[9,2]*, Flora M. Vaccarino[1,2,11,12,13,14]*

[1]Child Study Center, Yale University, New Haven, CT, 06520, USA.
[2]Program in Neurodevelopment and Regeneration, Yale University, New Haven, CT, 06520, USA.
[3]Department of Biomedical Engineering, Duke University, Durham, NC, USA;
[4]Center for Advanced Genomic Technologies, Duke University, Durham, NC, USA.
[5]Department of Pediatrics, Duke University, Durham, NC 27708 USA.
[6]Center for Alzheimer's and Related Dementias, National Institutes of Health, Bethesda, MD
[7]Department of Neurology, Yale University, New Haven, CT, 06520, USA.
[8]Brain Institute, Department of Neurology, University of Virginia, Charlottesville, VA, 22904, USA.
[9]Department of Quantitative Health Sciences, Center for Individualized Medicine, Mayo Clinic, Rochester, MN, 55905, USA.
[10]National Institute of Neurological Disorders and Stroke, NIH, Bethesda, MD 20892, USA
[11]Department of Neuroscience, Yale University, New Haven, CT, 06520, USA.
[12]Kavli Institute for Neuroscience, Yale University, New Haven, CT, 06520, USA.
[13]Yale Stem Cell Center, Yale University, New Haven, CT, 06520, USA.
[14]Lead Contact

†These authors contributed equally to this work
*Correspondence: flora.vaccarino@yale.edu, abyzov.alexej@mayo.edu

Summary

Cell differentiation is orchestrated by transcription factors (TFs) binding to enhancers, shaping gene regulatory networks that drive neuronal lineage specification. Deciphering these enhancer-driven networks in human forebrain development is essential for understanding the genetic basis of neurodevelopmental disorders. Through integrative epigenomic and transcriptomic analyses of human forebrain organoids derived from 10 individuals with autism spectrum disorder (ASD) and their neurotypical fathers, we constructed a comprehensive enhancer-driven gene regulatory network (GRN) of early neurodevelopment. This GRN revealed hierarchical regulatory transitions guiding neuronal differentiation and was experimentally validated via CRISPR interference (CRISPRi) and loss-of-function analyses. A subnetwork linked ASD-associated transcriptomic alterations to dysregulated TF activity, implicating FOXG1, BHLHE22, EOMES, and NEUROD2 as key regulators of excitatory neuron specification in macrocephalic ASD. These findings suggest that ASD disrupts enhancer-driven regulatory frameworks, altering neuronal cell fate decisions in the developing fetal brain.

Introduction

Fundamental cell fate decisions and regional specification during early human brain development underlie our larger brain size, cellular diversity, and cognitive abilities, but also our susceptibility to neurodevelopmental disorders, such as autism spectrum disorders (ASD). Brain organoids derived from human induced pluripotent stem cells (iPSC) are a multilineage model that emulates the dynamics of brain development in an individual's genetic background[1-3]. While several transcriptomic studies have charted lineage specific gene expression patterns of fetal human brain and brain organoids, less is known about how those lineages are specified by the non-coding genome, and specifically by enhancers, the main elements implicated in the modulation of gene expression[4]. Located at variable distances from gene promoters, enhancers are bound by specific transcription factors (TFs) which can modify chromatin conformation and interact with the promoter machinery to increase or decrease the expression of downstream genes [5-7]. TFs, enhancers and other types of regulatory regions have been described in the adult[8,9] and prenatal [10-12] human brain, but postmortem brain studies cannot capture the dynamic unfolding of developmental events and do not allow for experimental manipulation. We and other have started to chart enhancers location and activity during early brain development in both fetal human cortex and isogenic organoids [13] and a recent study has used the organoid approach to identify the regulatory events that drive early cell fate decisions between neural and non-neural cells [14]. Understanding the regulatory relationships between enhancers, TFs and gene expression during development remains an important step to understand the etiology of neurodevelopmental disorders.

In our recent study of cortical organoids from 13 families with idiopathic ASD with or without macrocephaly, we found by scRNA-seq analyses a strong imbalance in excitatory neuron lineages when comparing ASD probands to their neurotypical father[15]. In the present study we performed histone marks chromatin immunoprecipitation and sequencing (ChIP-seq) and parallel RNA sequencing analyses in iPSC-derived forebrain organoids from 10 out of those 13 families. Integrating enhancer activity with TF binding sites and gene expression on a genome-wide scale, we built a gene regulatory network (GRN), identifying enhancers and cognate TFs active during the progression of neurogenesis and the diversification of neuronal subtypes. By comparing enhancer activity and differential gene expression of individuals with ASD to their unaffected father as controls, we further delineated the regulome underlying the transcriptional alterations observed in ASD with and without macrocephaly.

Results

1. Building a gene regulatory network based on epigenome and transcriptome during forebrain organoid development

Study cohort. In the present study we characterize epigenomic and transcriptomic states of precursor cells and early neurons using iPSC lines from 10 idiopathic ASD individuals and their unaffected fathers differentiated into forebrain organoids and analyzed by scRNA-seq, ChIP-seq and bulk RNA-seq. The clinical information and genetic background of the individuals have been previously reported in a single cell transcriptome study of this cohort [15]; we now analyze ChIP-seq and bulk RNA-seq data collected in parallel to understand the regulatory events underlying the transcriptomic phenotypes observed in the ASD individuals. ASD probands were classified as "macrocephalic" if exhibiting head size above 90th head size percentile or as "normocephalic" if exhibiting normal head size using a normative dataset[16]. Since macrocephaly is often a family trait, the control fathers of macrocephalic probands were also macrocephalic (see clinical information in **Table S1**). The iPSC lines from all individuals were previously characterized by whole genome sequencing[15]; although some probands carried a variant affecting a gene associated with syndromic ASD, except for a large duplication, variants did not change the expression for the corresponding genes, and variants did not converge on the same genes across our idiopathic cohort (see Jourdon et al, 2023 for full description of the results).

All iPSC lines were differentiated into forebrain organoids and histone marks-ChIP-seq (H3K4me3, H3K27ac, H3K27me3 and H3K4me1), bulk RNA-seq and scRNA-seq were concurrently performed at terminal differentiation day 0 or TD0 (corresponding to 20 days after neural induction of the iPSC lines), TD30 and

TD60 (**Fig. 1A**, **Table S1**). We then developed a pipeline that integrated this multi-omics data collected in parallel into a *regulatory network* of human forebrain organoid development (**Fig. 1B, Methods**). First, integrated annotation of the genome using a ChromHMM 9-states model[17] for ChIP-seq data identified putative promoters, enhancers (~360,000), and silent chromatin regions (**Fig. 1C-D).** Enhancers were then linked to potential target genes by proximity to promoters (20 kb) or by reported distal interactions identified in human fetal brain Hi-C datasets[18-20] **(Fig. S1A).** Altogether, 173,437 gene-linked enhancers (GLEs) were mapped across all samples (**Fig. S1B-E, Table S2**).

GLEs were then linked to TFs by the presence of a TF binding site (TFBS) motif in their sequence (**Fig. S1E-F)**. Next, significant correlations between GLE activity (H3K27ac reads) and expression of the linked gene (RNA reads) across samples were used to retain the most functionally relevant links and infer the direction of the regulation. Both activating (positive correlation) and repressing (negative correlations) regulatory relationships linking TFs to enhancers, and enhancers to their downstream genes were retained (**Fig. 1B**, **Fig. S2A,B**). Repressive GLE-genes regulatory relationships (n=1,556) were much fewer than activating ones (n=6,794). Repressive and activating TF-GLE regulatory relationships were similar in numbers, suggesting that ~50% of developmental TF could act as repressors. While we could not exclude that part of this negative correlation could be explained by coincidental absence of activators, repressor TFs are known to be able to induce histone deacetylation and inhibit the recruitment of basal machinery without inducing chromatin compaction[21]. We therefore decided to incorporate both positive and negative TF-to-enhancer regulatory links in our network analysis.

All retained links were integrated into a TF-enhancer-gene network connecting 373 TFs, 42,035 GLEs, 6,501 protein coding genes and 1,690 long non-coding RNAs (lncRNAs) (**Table S2, T2-3**). In such network, active enhancers are pivotal elements in the upstream regulatory network of any expressed gene, some with complex regulatory cascades (**Fig. 1E-F**, **Fig. S3**). Compared to initial set of GLEs called, the subset of GLEs included in the GRN showed a significantly higher overlap with sets of known enhancers in human [13,22,23] (71% overlap with ENCODE candidate regulatory elements), confirming the relevance of using correlation with transcription levels to better refine regulatory elements identification (**Fig. 1H)**. Many identified GLEs also overlapped with open chromatin regions identified by bulk and single-cell ATAC-seq assays performed on human fetal brain or brain organoids in published datasets [10,14,24,25] (43% overlap, **Fig. 1I**). This degree of overlap was remarkable considering that ChIP-seq and ATAC-seq identify regulatory regions based on histone post-translational modification vs accessible chromatin region.

To capitalize on this characterization of enhancer-centered regulatory cascades, we derived a reduced representation in the form of a gene regulatory network (GRN), where TF were directly connected to downstream gene(s) when one or several intermediate functional GLE(s) linking them was identified (**Fig.1E-F, Fig. S2C**). We pruned 13.3% of such links by requiring a significant correlation not only between TF expression and GLE activity and GLE activity and target gene(s), but also between expression of the TF and downstream gene and used the obtained correlation coefficient to infer both the strength and the activating or repressing nature of the TF-to-gene regulatory action (**Methods)**. The resulting GRN consisted of 330 upstream TFs regulating 5,067 downstream transcripts, encompassing 4,034 protein-coding genes and 1,023 lncRNAs (**Fig. 1G, Table S3**). As we incorporated data from both ASD probands and controls to increase confidence in correlation inference, we verified that ASD diagnosis had a limited effect on the variance of gene and TF's expression and was unlikely to drive correlation results (**Fig. S2D,E**), ensuring that the GRN was representative of molecular events driving typical neurogenesis. We found a limited overlap between the obtained GRN and a published regulatory network derived by integrating scATAC-seq and scRNA-seq conducted on stem cells, early progenitor cells and organoids [14] (2.3% of TF-gene regulatory edges in common). The inclusion of earlier time points and methodological differences suggested that the two networks described connections of different sets of TFs (200 TFs in common or 23.5% of the union) and genes (823 targets or 12% of the union) (**Fig. S4C-F**). However, the large majority of the common edges (239/249) show consistent measures in TF-to-gene correlation estimates between the two studies, suggesting that both networks captured the same regulatory interactions (**Fig. S4F**). Ultimately, those different networks could be used in complement to chart a more complete view of regulatory actions during development.

150 The GRN was built around TFs and their ability to activate and repress a set of targeted genes, also
151 known as their *regulons*. To identify how TFs structured the GRN, we evaluated the overlap between the
152 regulons of each pair of TFs across the network and measured how similar or opposite was their inferred actions
153 on shared targets (**Fig S4**). This delineated an *interactome* of TFs, identifying for each TF a set of preferential
154 collaborators and competitors that tended to regulate genes through either identical or separates enhancers.
155 Strongest interactions occurred not only between TFs with closely related binding motifs families (driven in part
156 by similarity in targeted enhancer sites), but also across major brain regulators which are known to coregulate
157 genes expression (**Fig. S4A**). For instance, the interactome of the TFs EOMES revealed a preferential
158 collaboration with NEUROG2, NEUROD2 or MEF2C and a competition with FOXB1, LHX6 or ZNF823
159 across several targets in the GRN. Other examples included FOXP2 collaboration with ZNF548 and competition
160 with TEAD4; or TBR1 collaboration with NFIB and ESR2 and competition with ZNF823 (**Fig. S4B**).
161 Altogether, the built GRN integrated enhancer identification with gene expression to chart the regulatory effects
162 and interactions of TFs in our organoid model (see GRN in **Table S3**).
163

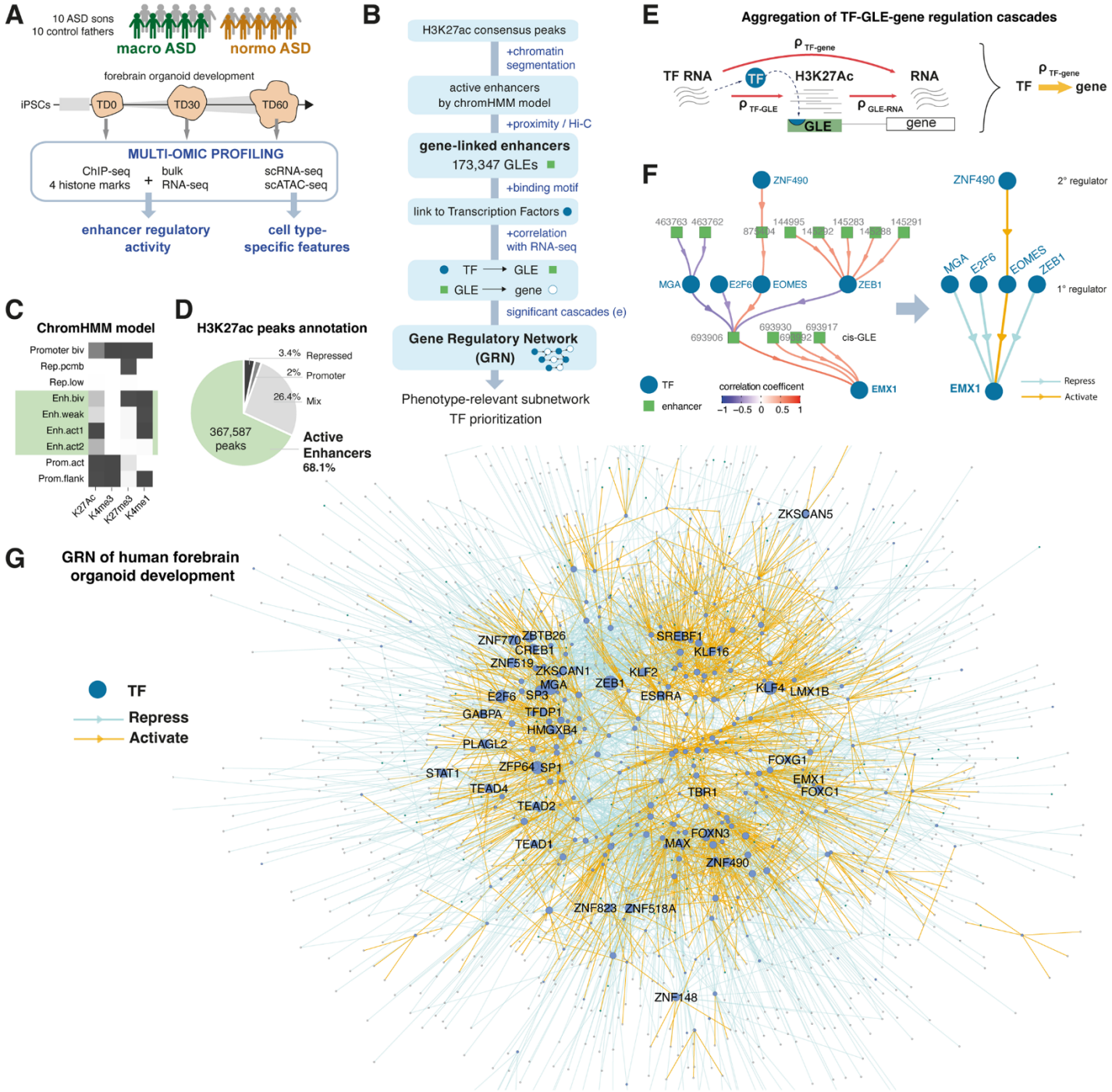
A
10 ASD sons
10 control fathers
macro ASD
normo ASD
forebrain organoid development
iPSCs
TD0
TD30
TD60
MULTI-OMIC PROFILING
ChIP-seq
4 histone marks
bulk
RNA-seq
scRNA-seq
scATAC-seq
enhancer regulatory activity
cell type-specific features
B
H3K27ac consensus peaks
+chromatin segmentation
active enhancers by chromHMM model
+proximity / Hi-C
gene-linked enhancers
173,347 GLEs
+binding motif
link to Transcription Factors
+correlation with RNA-seq
TF → GLE
GLE → gene
significant cascades (e)
Gene Regulatory Network (GRN)
Phenotype-relevant subnetwork
TF prioritization
C
ChromHMM model
Promoter biv
Rep.pcmb
Rep.low
Enh.biv
Enh.weak
Enh.act1
Enh.act2
Prom.act
Prom.flank
K27Ac
K4me3
K27me3
K4me1
D
H3K27ac peaks annotation
3.4% Repressed
2% Promoter
26.4% Mix
367,587 peaks
Active Enhancers 68.1%
E
Aggregation of TF-GLE-gene regulation cascades
TF RNA
TF
H3K27Ac
RNA
GLE
gene
TF → gene
F
ZNF490
MGA
E2F6
EOMES
ZEB1
cis-GLE
EMX1
TF
enhancer
correlation coefficient
2° regulator
1° regulator
Repress
Activate
G
GRN of human forebrain organoid development
TF
Repress
Activate
ZKSCAN5
ZNF770
ZBTB26
CREB1
ZNF519
ZKSCAN1
MGA
SP3
E2F6
GABPA
TFDP1
HMGXB4
PLAGL2
ZFP64
SP1
STAT1
TEAD4
TEAD2
TEAD1
ZEB1
SREBF1
KLF16
KLF2
ESRRA
KLF4
LMX1B
FOXG1
EMX1
FOXC1
TBR1
FOXN3
MAX
ZNF490
ZNF823
ZNF518A
ZNF148
H
fraction of peaks from this study
Overlap with known human enhancer
all enhancers
GLE
GLE in GRN
Screen (ENCODE) 46.7% 171,805 52.1 90,386 71.2 29,928
Genehancer (ENCODE/VISTA/FANTOM/Ensembl) 49.4 181,414 54.8 95,044 71.2 29,906
Amiri et al. 2020 fetal brain +organoid ChIP-seq-GLE 15.9 58,539 32.3 56,028 44.4 18,665
I
Overlap with fetal brain/organoid ATAC-seq data
any overlap = 43% of all GLE
Intersection with GLE
11.5%
8.7%
5.8%
2.9%
0
22,008
20,631
14,014
12,716
1,297
1,102
974
697
486
485
170
134
22
15
4
Trevino et al. 2020
Ziffra et al. 2021
Markenscoff-Papadimitriou et al. 2020
cell-specific in Fleck et al. 2022
60k 40k 20k 0

Figure 1: Building a regulatory network during forebrain organoid development anchored around the identification of active enhancer elements.

A. Study design with multi-Omic characterization of forebrain organoid development in 20 individuals including ASD individuals with or without macrocephaly ("macroASD", head circumference > 90th percentile of the population, "normo ASD" otherwise).

B. Data integration pipeline to generate the GRN (see **Methods**). It incorporates enhancer-gene linkages from proximity and Hi-C, TFBS identification, and correlation of enhancer activity with expression of upstream TF(s) and downstream gene(s). The final step consists in the derivation of a GRN through aggregation of the TF-enhancer-gene cascades (see **E**).

C. The 9-states model of genome annotation built using the 4 chromatin marks ChIP-seq data from this study. Four enhancer states were then merged into an "active enhancer" state. Enhancers profiles were essentially characterized by H3K27Ac without H3K4Me3 activity.

D. Diagram showing the proportion of each main chromatin state identified in (**C**) for all H3K27ac consensus peaks.

E. Schematic of the aggregation strategy validating the intermediate role of enhancers through concordant correlation at the RNA level between TF and downstream genes (see also **Fig. S2**). Regulatory actions were then summarized to build the TF-gene GRN, conserving only the correlation between TF and gene in the final network. Blue arrows=negative and red arrows= positive correlation (ρ).

F. Upstream enhancer regulatory network of the gene EMX1. Arrows indicate regulatory link between TFs and their bound GLEs (in green with unique ID from **Data S2**) and links from GLE to their downstream gene in *cis*. Colors of the arrows show correlation level between the linked elements. Note the four-steps distance between the TF ZNF490 and EMX1 expression. The corresponding TF-gene network is plotted on the right using TF-gene RNA level correlation as link weight (two-sided Spearman's correlation FDR corrected p-value < 0.05).

G. Visualization of the central component of the GRN inferred from the enhancer regulatory network, plotted by Kamada-Kawai graph layout. Genes connected by repressive regulation (i.e., $\rho_{TF-RNA} < 0$) are further apart than genes connected by activating regulation (see **Methods**). By construction, TF (blue dots) are central element of the GRN, each connecting in their regulon 1 to 1,047 downstream genes (small grey dots). Top 50 TF by regulon size (dot size) and salient TFs from our study are named.

H Fraction of all enhancers regions ("All Enh."), gene-linked enhancer ("GLE") and regulatory GLE ("reg-GLE", i.e., GLE significantly correlated in activity with gene expression, FDR < 0.01, **Data S2**) that overlap with reported human enhancers from 3 sources [13,22,23]. Dot shows percentage enhancer from our study overlapping with each source, corresponding number of peaks is indicated below. All overlaps increased significantly from "All Enh." to "GLE" to "reg-GLE" (p-values of one-tailed Fisher exact test < 2.2×10^{-16}).

I. Upset plot showing the intersection between GLE from this study and peaks identified in published bulk and single-cell ATAC-seq data from human fetal brain or brain organoid models [10,14,24,25].

202 ## 2. Identification of master regulators behind neurogenesis progression and cell type specification

203 To explore how the enhancer-centered GRN captured regulatory events of human neural development,
204 we next sought to identify the regulatory relationships central to the progression of neurogenesis. The GRN was
205 therefore subset to only include genes differentially expressed between TD30/60 and TD0 (i.e., late vs early,
206 termed timeDEGs) (**Fig. S5A-B, Table S4, T1**). Regulatory links in the GRN were then subset to include only
207 links where change in expression of upstream TF was susceptible to drive differential expression of the
208 downstream gene (**Fig. 2A, Methods**). This time transition subnetwork revealed two antagonizing groups of
209 TFs driving major expression changes during early development (**Fig. 2A**, **Fig. S6C**). To further rank TFs'
210 abilities to drive expression changes, we computed for each TF an *activity perturbation score* that measured
211 how its regulon was differentially affected between 2 conditions based on GRN prediction. The perturbation
212 score metric is detailed in **Fig. S6**, with positive, negative, and near-zero perturbation scores indicating
213 respectively, an increased, decreased or unchanged activity of the TF between two tested conditions. Applied to
214 timeDEG, this perturbation analysis revealed that increased activity of TBR1, FOXP2 and POU6F1 and
215 decreased activity of DMRTA1, FOSL1, and TEAD4 were driving gene expression changes across this time
216 transition (**Fig. 2B**). Interestingly, some TFs with low change in expression level across time points had high
217 activity perturbation scores (for instance ZNF490, SP1 or FOXN3). Such cases could stem from differences in
218 posttranscriptional modulation of the TF, influencing for instance its DNA- or protein-binding abilities, although
219 this could also result from expression changes in TFs acting on closely related regulons. The TD30 to TD60
220 transition, involving primarily an increase in neurogenesis, was driven by increased activity of TFs such as
221 BHLHE22, NEUROD2, ESRRA or BHLHE40 (**Fig. S6D,E**).

222 Organoids develop from aggregates of neural progenitors that generate a diversity of neurons over
223 time[3,26]. Using scRNA-seq data, we have shown that our organoid method generated a diversity of forebrain
224 neuron fates (**Fig. 2C**) and that the proportion of different cell types tended to vary between organoids from
225 different individuals [15]. Since bulk-level gene expression in organoids is strongly driven by changes in cell type
226 composition, we hypothesized that the GRN captured in part the regulatory events driving variations in cell
227 fates. Indeed, we observed that many timeDEGs had cell type-specific expression in scRNA-seq data (**Fig. 2D,**
228 **Fig. S5A-C**), including many TFs drivers of time transition identified from the GRN (**Fig. 2B**). Coherently,
229 TFs' activated regulons tended to be co-expressed in the same cells as their upstream TF, while repressed part
230 of their regulon had often inverted expression pattern across cells (**Fig. 2D**, **Fig. S5C**). This suggested that many
231 central TFs in the GRN are driving binary choices between cell type identities or states. We therefore applied
232 the perturbation activity score metric to cell-type specific DEGs (**Table S5**) to evaluate each TF's capacity to
233 drive cell type-specific expression pattern and identify putative activators and repressors of specific cell fates
234 (**Fig. 2E**). As expected, many TFs controlled the distinction between neurons and progenitor cells (e.g., FOXP2,
235 SOX4, TFAP2E) upregulating general neuron fate and repressing radial glia, while some TFs were preferentially
236 regulating genes expressed by a particular neuronal subtype. Among the latter, EOMES, BHLHE22,
237 NEUROD2, and NFIC were the strongest activators of excitatory neurons of the dorsal cortical plate (EN-DCP),
238 while E2F6, TCF7L2 and POU2F1 were the strongest repressors of that fate, consistent with mouse loss-of-
239 function studies [27,28].

240 To evaluate how cell type-specific regulatory events were captured in data derived from bulk-level ChIP-
241 seq, we intersected our list of GLEs with open chromatin peaks called from 29 scATAC-seq samples collected
242 from the same organoid preparations (**Table S2**). We found that 40.1% of GLEs overlapped with an ATAC-seq
243 peak identified in a cell type or shared across cells (**Fig. 2F**). Furthermore, activating GLE-to-gene regulatory
244 links from the bulk GRN were enriched in cell type-specific links (i.e., cases where the GLE overlapped a
245 scATAC-seq peak and the linked gene showed increased expression in the same cell type in scRNA-seq data),
246 suggesting that the bulk-derived regulatory network captured cell type-specific regulatory events and increasing
247 confidence in our characterized enhancer elements. This enrichment was more significant for neuronal cell types
248 and particularly for EN-DCP (**Fig. 2G**). Altogether, these analyses suggested that identification of enhancers
249 from bulk epigenome along the developmental timeline captured the complex regulatory events underlying the
250 development of a multilineage system.

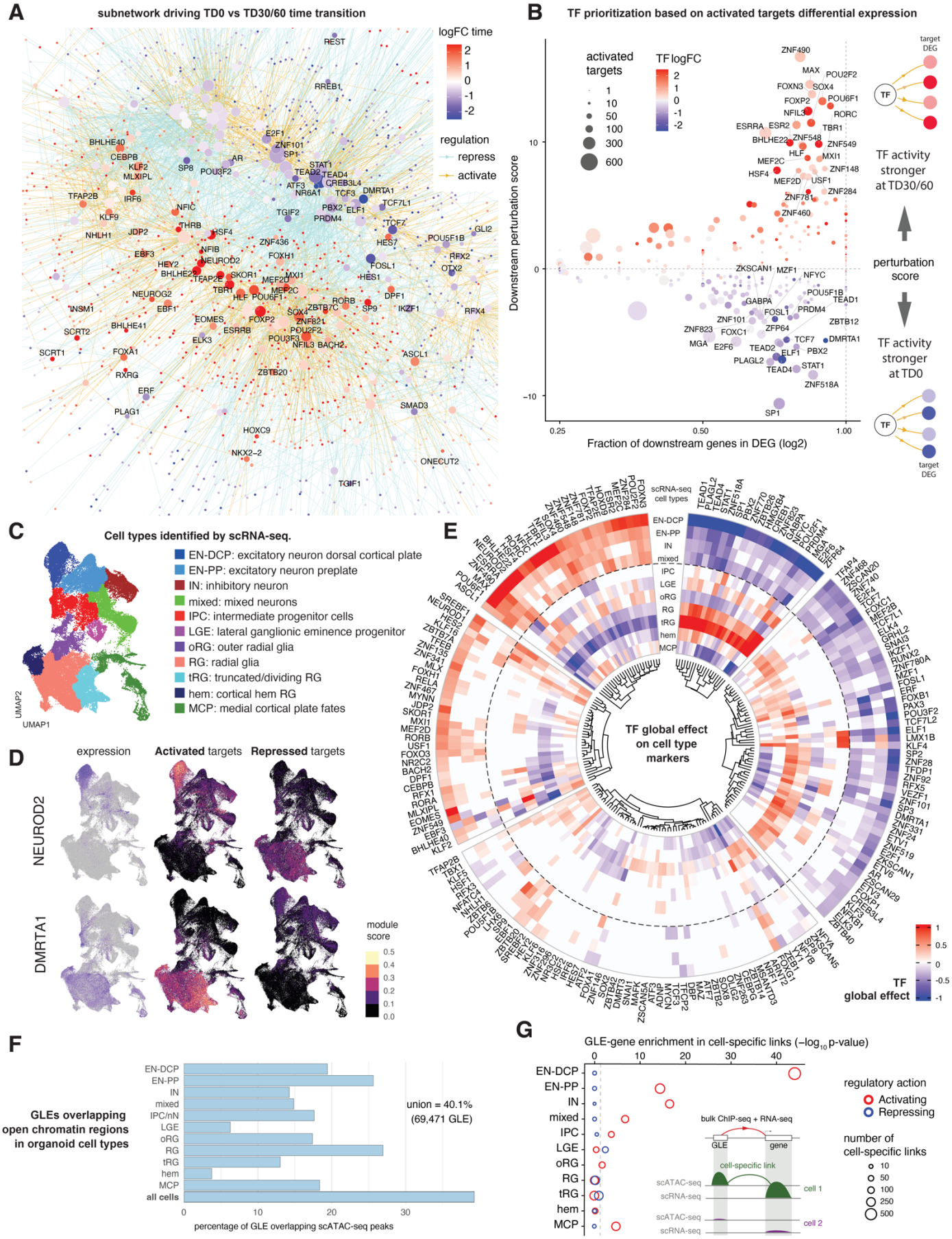
A
subnetwork driving TD0 vs TD30/60 time transition
logFC time
regulation
repress
activate
B
TF prioritization based on activated targets differential expression
activated targets
TF logFC
Downstream perturbation score
Fraction of downstream genes in DEG (log2)
target DEG
TF
TF activity stronger at TD30/60
perturbation score
TF activity stronger at TD0
C
Cell types identified by scRNA-seq.
EN-DCP: excitatory neuron dorsal cortical plate
EN-PP: excitatory neuron preplate
IN: inhibitory neuron
mixed: mixed neurons
IPC: intermediate progenitor cells
LGE: lateral ganglionic eminence progenitor
oRG: outer radial glia
RG: radial glia
tRG: truncated/dividing RG
hem: cortical hem RG
MCP: medial cortical plate fates
UMAP2
UMAP1
D
expression
Activated targets
Repressed targets
NEUROD2
DMRTA1
module score
E
scRNA-seq cell types
TF global effect on cell type markers
TF global effect
F
GLEs overlapping open chromatin regions in organoid cell types
union = 40.1% (69,471 GLE)
percentage of GLE overlapping scATAC-seq peaks
G
GLE-gene enrichment in cell-specific links (−log10 p-value)
regulatory action
Activating
Repressing
number of cell-specific links
bulk ChIP-seq + RNA-seq
GLE
gene
cell-specific link
scATAC-seq
scRNA-seq
cell 1
cell 2

Figure 2. Master regulators driving neurogenesis and cellular diversity in forebrain organoids

A. Time transition subnetwork built from the GRN by retaining significant timeDEGs (TD30+60 vs TD0, $|\log_2 FC| > 0.25$ and FDR < 0.01) and concordant links connecting them. Activating edges (yellow) need to connect timeDEGs with same direction of change and repressive edge (cyan) timeDEGs with opposite directions of change. Top TFs ranked by logFC are named. Kamada-Kawai layout with distances proportional to the direction and strength of the regulation as in **Fig. 1G**.

B. Dot plot showing the fraction of TF's targets that are timeDEG (x-axis) and the TF activity perturbation score (y-axis, schematic). Dot color shows the TF's own $\log_2 FC$ in timeDEG. Dot size=regulon size in the GRN. The perturbation score ranks each TF's ability to drive the expression changes of its regulon (here, across time) and is computed from GRN prediction and DEG results for the downstream target only. As shown by yellow arrows in right side schematic, only activating relationship were used for the perturbation score in this plot. Top 25 TF by activity perturbation score are named (see **Methods** and **Fig. S6**).

C. UMAP plot colored by cell types identified in 72 scRNA-seq samples from TD0, 30 and 60 organoids [15] of the same individuals used for this study.

D. UMAP plots colored by expression level for the TF NEUROD2 and DMRTA1 (left panels, blue=high, grey=low). To infer if TF's targets also presented cell-type specific expression, the respective downstream "activated targets" and "repressed targets" of each TF's regulon were used to derive a module expression score in the scRNA-seq data and positive module scores per cell are plotted in the UMAP (see also **Fig. S5C**).

E. Circular heatmap showing the global effect of each TF on cell type-specific gene expression quantified by scRNA-seq (see **Data S5** for cell type markers). Results for each cell type plotted as concentric circles. TF's global effect is a perturbation score applied to cell-type DEGs (as in **B**, **Methods**). Results are grouped by k-mean clustering (k=5) and hierarchical clustering (Euclidean distance, complete method).

F. Fraction of all GLEs that intersect with scATAC-seq peaks in organoids (overlap with peaks identified in at least 3 out of 29 scATAC-seq samples, see **Fig. S5** for scATAC-seq peaks overlap and QC results). "all cells" = peaks called using all cells. Cell type annotations were identified by label transfer using scRNA-seq from **C** as reference.

G. Enrichment of cell type-specific regulatory relationships (cell-spe.links) among all enhancer-gene regulatory relationships identified (**Table S2,T3**). *Cell-specific links* were defined as cases where the enhancer overlaps with scATAC-seq peaks (>= 3 samples) and the linked gene is a cell type-specific marker of the same cell type. Enrichment was calculated separately for activating and repressing enhancer-gene links (red and blue circles, respectively). p-value of one-tail Fisher exact test reported.

285 ## 3. ASD probands show dysregulation in TF regulators of excitatory and inhibitory neuron specification

286 We have previously shown by scRNA-seq that organoids derived from macrocephalic ASD individuals
287 in the present cohort (macroASD) showed an increase in EN-DCP cell proportions and gene expression as
288 compared to their unaffected fathers, whereas normocephalic ASD individuals (normoASD) showed a
289 diametrically opposite phenotype [15]. Here, by analyzing paired ASD versus control-father DEGs by bulk RNA-
290 seq (pDEG in **Fig. S7**) and differentially active enhancers (pDAE in **Fig. S8A**) we confirmed those opposite
291 phenotypes at the bulk transcriptomic and epigenomic levels (n=4 macroASD pairs and n=5 normoASD pairs,
292 analyzed at TD0 and at TD30 + TD60 (merged together to increase power), see **Methods** & **Table S4, T1-2**).
293 As in the scRNA-seq dataset, most DEGs were changed either in a cohort-specific manner or in opposite
294 directions, with only 13 concordant pDEGs between the macroASD and normoASD cohorts (out of 641 pDEGs
295 in either cohort at TD30/60, **Fig. S7C**). Bulk transcriptome data reproduced the upregulation and
296 downregulation of gene markers of EN-DCP cells in macroASD and normoASD, respectively (**Fig. S7B-D**).
297 This was further supported by an upregulation of enhancers upstream of several of those EN-DCP genes in
298 macroASD pDAE (including of *EMX1*, *NEUROG2*, *NFIA*, and *LHX2*) (**Fig. S8A,B)**. In addition to this EN
299 phenotype, a strong downregulation in genes related to the inhibitory neurons (IN) lineage (e.g., *DLX*-genes and
300 *GSX2*) was observed at both TD0 and TD30/60 in macroASD pDEG (**Fig. S7A-D**).

301 To deconvolute the regulatory drivers of ASD-associated changes, we identified the upstream TFs of
302 macroASD pDEGs in the GRN (**Fig. 3A**). This **macroASD subnetwork** comprised 96 pDEGs (out of 420)
303 controlled by 102 TFs, of which 19 were pDEGs themselves (**Fig. 3A**). We then applied TF activity perturbation
304 analysis (**Fig. S6**) to systematically rank each TF's ability to drive differential expression of its downstream
305 targets in macroASD. This analysis highlighted an "EN regulatory hub" composed of the master regulators
306 BHLHE22, EOMES and FOXG1 as the strongest drivers of the macroASD pDEG (**Fig. 3B**) which were all
307 strongly associated with EN-DCP fates regulation (**Fig. 2E**). BHLHE22, EOMES and FOXG1 acted on several
308 downstream TFs controlling EN-DCP fate such as EMX1, LHX2, ZBTB18 and BCL11A (**Fig. 2E, 3A,B**).
309 While we had lower sensitivity to detect pDAEs than pDEGs, in several cases the intermediate enhancer
310 connecting the TF to the downstream pDEG in the GRN was itself a pDAE (**Fig. S8B**). For instance, in
311 macroASD, the upregulation of the TF *ZBTB18* could be associated with the upregulation of two of its enhancers
312 (ID: 123747, 124166) themselves also bound by the TFs BHLHE22, TBR1 and TFAP2C, three upregulated
313 pDEGs. Similar intermediate pDAEs linked FOXG1 to *BCL11A*, FOXG1 to *LHX2*, and EOMES to *EMX1* (**Fig.**
314 **S8B**). Such cases identify potential "propagation paths" of the phenotype where TFs' expression changes caused
315 epigenomic changes in targeted enhancer elements and ultimately differential expression of secondary
316 downstream targets. In agreement with the observed decreased in GABAergic interneuron (IN) genes in
317 macroDEGs, the known inhibitory lineage TFs ASCL1 and LHX6 ranked among the top driver TF with
318 decreased activity in macroASD (**Fig. 3B**).

319 Similarly, the **normoASD subnetwork** placed 85 pDEGs (out of 315 pDEG at TD30/60) under the
320 control of 103 upstream causative TFs. In normoASD, the "EN hub" composed of the master regulators
321 BHLHE22, EOMES and FOXG1 showed strong decrease in activity, causing a secondary downregulation of
322 *EMX1*, *LXH2, NEUROG2, TBR1, ZBTB18, BCL11A,* and *NEUROD6* (**Fig. 3C,D**). These TFs often co-regulated
323 each other, with, for instance, LHX2 downstream of EOMES and FOXG1, and ZBTB18 controlled by both
324 BHLHE22 and TBR1. Interestingly, the top three TFs with increased activity in normoASD (i.e., LMX1B,
325 FOXB1 and FOXA1, **Fig. 3D**) were direct repressors of FOXG1 and were affected in an opposite way in the
326 macroASD cohort. Taken together, the GRN identifies opposite dysregulation of two triads of co-regulated TFs
327 (BHLHE22, EOMES and FOXG1 against LMX1B, FOXB1 and FOXA1) as the strongest drivers of the opposite
328 transcriptomic phenotypes observed in our macro- and normo-ASD cohorts. Those results reinforce that
329 organoids from these cohorts of ASD probands revealed divergent transcriptomes as well as epigenomes.

330 To expand our study beyond ASD idiopathic individuals, we performed a similar analysis to explore the
331 regulation and interconnection of genes associated to rare variants in ASD (SFARI genes). The built GRN can
332 allow to understand how genes carrying rare ASD mutations interact together to perturb brain development. For
333 instance, using the list of identified enhancers and their upstream networks (**Data S2**), we could identify the
334 upstream enhancers and TFs that regulate the SFARI risk genes CHD3 (**Fig. 4A**). Associating upstream regions

335 de facto extends the genomic regions of interest for the identification of disruptive variants of any given risk
336 gene to noncoding regions or indirectly associated coding regions. The GRN could also be used to identify paths
337 of downstream regulatory convergence between ASD risk genes. We identified regulatory relationships
338 associating 348 ASD-associated risk genes identified in SFARI (out of ~1000) (**Fig. 4B**). Risk genes were
339 preferentially associated in the GRN (Fisher exact test two-sided p-value = 0.0015), notably because they
340 included 33 highly interconnected TFs. Some TF risk genes such as BCL11A were downstream of important
341 TF such as FOXP2, TBR1 or FOXG1, which are part of the EN regulatory hub implicated in the idiopathic ASD
342 subnetwork (**Fig. 3A**).

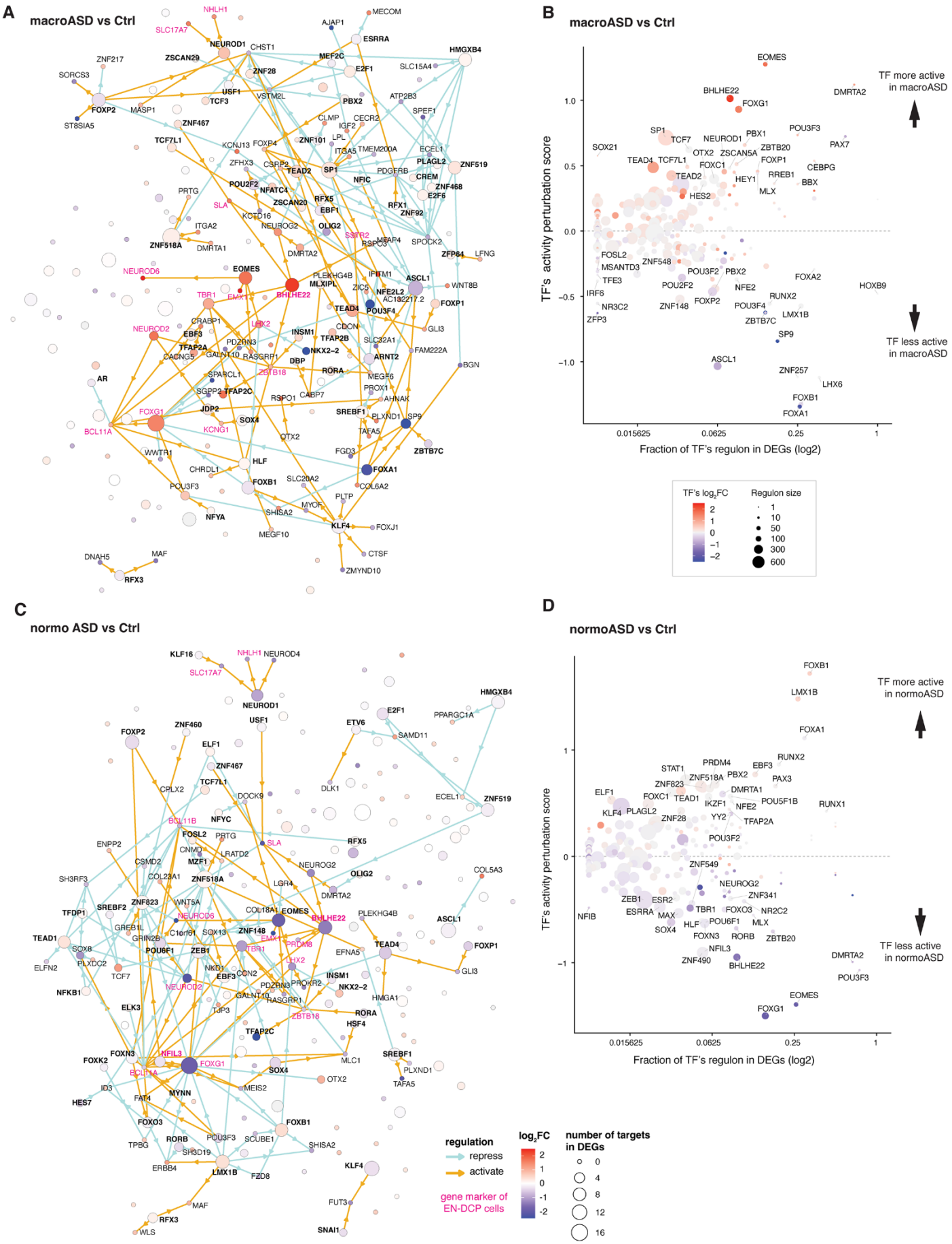
A
macroASD vs Ctrl
B
macroASD vs Ctrl
TF more active in macroASD
TF less active in macroASD
TF's activity perturbation score
Fraction of TF's regulon in DEGs (log2)
TF's log2FC
Regulon size
C
normo ASD vs Ctrl
D
normoASD vs Ctrl
TF more active in normoASD
TF less active in normoASD
regulation
repress
activate
gene marker of EN-DCP cells
log2FC
number of targets in DEGs

343

Figure 3. ASD probands have head-size cohort-specific alterations of the regulatory network coordinated by central transcription factors like FOXG1.

A,C. TF-to-gene GRN subnetwork depicting pDEGs (paired DEGs between ASDs and control fathers using TD30 and TD60 bulk RNA-seq expression level) and their upstream TFs for macroASD (**A**) and normoASD (**C**). Color of the genes represents expression change, while color of arrows represents the regulatory action (activation/repression) from the GRN (**Fig. 1G**). Genes are disposed identically in **A** and **C**. Dot size show number of targets in the resulting network. Gene markers of EN-DCP cells from scRNA-seq data are in red.

B,D. TF ranking based on their activity perturbation scores against macroASD pDEGs (**B**) and normoASD pDEGs (**D**). TFs are plotted based on the fraction of their downstream targets that are significantly pDEGs (x-axis) versus the TF's activity perturbation scores (y-axis) which evaluates each TF based on how strongly its predicted effect in the GRN (i.e., activation/repression) accounts for the observed pDEGs in its regulon. Dot colored is the log2FC value of the TF itself (ASD vs Ctrl), dot size= regulon size.

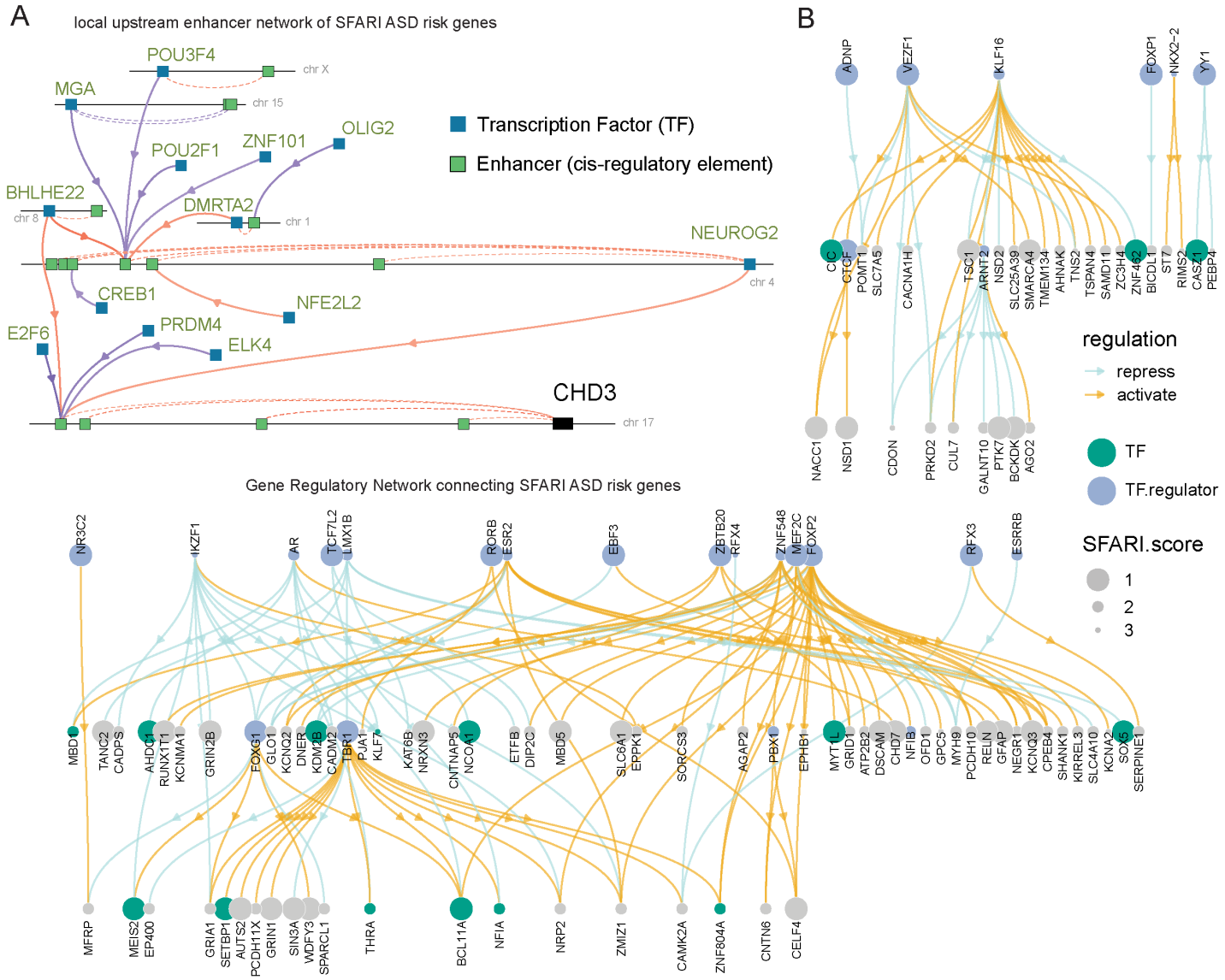

Figure 4 regulation and interconnection of known ASD risk genes

A. Example of upstream enhancer subnetwork for the ASD risk gene and chromatin modifier CHD3. Enhancers (green boxes) are connected to their downstream genes by dashed lines. TF (blue boxes) are connected to their downstream enhancer targets by arrows (red=activation, blue=repression). When in turn TF have themselves an enhancer controlling their expression, it is indicated on the linear genome. Enhancers are positioned at scale in the linear genome (their width is not represented, chromosome number is indicated, see **Data S2**,T4 for positions). Note the 6 degrees-separation between CHD3 expression and the TF OLIG2.

B. GRN restricted to links connecting 348 ASD risk genes (risk score indicated by size, with score=1 more confidently associated to ASD as defined by SFARI database).

368 ## 4. Enhancer cross-validation using CRISPRi

369 To validate our ability to identify enhancers using ChIP-seq and functionally confirm their downstream targets,
370 we applied CRISPR interference (CRISPRi) to our organoid system (**Fig. 5A**). We used a nuclease-deactivated
371 dCas9 fused to the Zim3 KRAB (Krüppel-associated box) domain, which recruits endogenous factors that
372 trimethylates histone H3 on Lys9 (H3K9me3), silencing the activity of targeted regulatory element [29,30]. We
373 generated an iPSC line with constitutive expression of Zim3-*dCas9*, a mScarlet reporter, and a hygromycin
374 selection cassette by PiggyBac transfection of the iF53 vector in a male control iPSC line (RDH913-03#9)
375 followed by hygromycin selection (**Figure S9A; Methods)**.

376 We constructed a gRNA lentiviral library to target 104 loci of interest, selecting multiple gRNAs per target locus
377 [31,32], **Methods**). This included 94 putative enhancer loci (enh-gRNA; median 10 gRNAs per locus, range 6-10)
378 selected from our study among the 173,437 GLEs initially identified (**Fig. 1B, Table S2**). It also included
379 gRNAs targeting the promoter regions (prom-gRNA) of 6 TFs (*BHLHE22, FOXG1, EOMES, NEUROD2,*
380 *LHX6, LXM1B;* 10 gRNAs per gene) and 4 positive control genes (*GRN, CDH2, TFRC, UBQLN2;* 3 gRNAs
381 per gene) previously shown to be efficiently repressed by CRISPRi in iPSC-derived neurons [33] to evaluate the
382 efficacy of CRISPRi. The library included ~10% of non-targeting gRNAs as negative controls (scrambled
383 sequences), for a total of 1079 gRNAs (**Table S6**). This gRNA library was transduced by lentivirus into the
384 Zim3-dCas9 iPSC line at high multiplicity of integration (MOI of ~5), as CRISPRi can be efficiently multiplexed
385 to test multiple gRNAs per cell to reduce cost[34]. After puromycin selection, the gRNAs+Zim3-dCas9 line was
386 differentiated into forebrain organoids and cells were analyzed by scRNA-seq at TD0 (~10k cells) to validate
387 the quality of the preparation. The majority of cells mapped to cell types previously described at this stage [15],
388 suggesting that the Zim3-dCas9 and gRNA lentiviral library integration did not alter the capability of the
389 RDH913-03#9 iPSC line to differentiate toward forebrain (**Figure S9B,C,D**). The downregulation of positive
390 control genes and *FOXG1* in the respective gRNA-carrying cells demonstrated that the Zim3-dCas9 system
391 efficiently silenced targeted chromatin regions and decreased gene expression (**Fig. S9E**).

392 The perturbation of targeted enhancers and TFs was then assessed at TD30 with high cell coverage (6 scRNA-
393 seq libraries, with a total of ~103k cells passing QC). After unsupervised clustering, cells were mapped to our
394 scRNA-seq reference [15] identifying forebrain RG and its subtypes, IPC/nN, EN-DCP, IN, and medial cortical
395 plate (MCP) cells (**Fig. 5B and S9F**). Cells contained a median of 7 gRNAs per cell (**Fig. 5C**) and ~95% of the
396 library's gRNAs were represented in the cell population at various frequencies, with a median of 343.5 cells per
397 gRNA (**Fig. 5D**). For each gRNA, differential expression was tested for genes in a 1Mb window around the
398 targeted locus using SCEPTRE [35] (see **Methods**) comparing cells expressing the gRNA to all other cells (**Fig.**
399 **5E, S9G,H**). Genes downregulated by at least 2 independent gRNAs targeting the same enhancer were
400 considered as validated cis-activated genes targeted by that enhancer (with differential expression meeting
401 FDR<0.1 significance, and no gRNA with significant discordant upregulation). We excluded cases where the
402 gRNA was located inside the downregulated gene body as gRNA-Cas9 binding could have directly disrupted
403 Pol2 elongation. This conservative analysis identified at least one downregulated target gene for 69 out of 94 of
404 the putative enhancer loci tested (**Table S6**), validating the presence of an enhancer element at those GLE loci
405 initially identified in our analysis.

406 To compare the results of CRISPRi to GLE-gene regulatory links identified during GRN construction based on
407 correlation of enhancer activity with expression of downstream gene(s) (**Fig. 1**), we focused on 22 GLE loci
408 with significant downstream gene(s) identified in both experiments, comparing 32 GLE-gene links tested in
409 both experiments (**Fig 5F-G**, **Methods**). Among those, 15 GLE-gene activating links in the GRN showed
410 concordant results in CRISPRi (validated regulatory link), corresponding to a 46.8% intersection rate between
411 tested enhancers across the two experiments (**Fig. 5H**). One link was found to have opposite direction of
412 regulation between the two experiments, while the remaining 17 links were called only by one approach.
413 Validated loci included enhancers activating important genes for EN-DCP neurogenesis including *NEUROD6*,
414 *EMX1*, *NEUROG2* and *ZBTB18*. Aside from identifying downstream targets of targeted enhancers, we also
415 identified 5 loci for which the gRNA presence induced shifts in cell composition, including the promoters of
416 *FOXG1* and *EOMES* (**Fig. 5I**), supporting that the perturbed genes were involved in organoid patterning, lineage
417 definition, and/or neurogenesis. The disruption of *FOXG1* expression created a major shift towards medial and

418 preplate cell types (**Fig S9I**). *EOMES* disruption appeared to redirect cells from EN-DCP to EN-PP, concordant
419 with the role of EOMES in indirect neurogenesis and IPC function in mouse studies[36]. To identify potential
420 downstream targets of TF perturbed by CRISPRi, we merged all the gRNAs affecting the same TF (promoter-
421 gRNA or enhancer-gRNA affecting gene expression) and tested for genome-wide differential expression
422 between cells with or without the tested gRNA, globally or at the cell type level (**Methods**). Although this
423 analysis cannot parse between direct and secondary effect of the CRISPRi-induced TF's downregulation and
424 focused on genes expressed in this particular experiment only, it validated several downstream targets of
425 EOMES, BHLHE22, as well as targets identified for ZBTB18 and NEUROG2 in the GRN (**Fig. 5J**). For
426 FOXG1, out of 111 GRN-predicted FOXG1 targets, 76 were expressed in the CRISPRi assay, of which 35 were
427 significantly differentially expressed, resulting in a validation rate of 46%.

428 To our knowledge, this is the first CRISPRi screen in forebrain organoids. While cost and technical limitations
429 make screening larger gRNA libraries challenging, the successful CRISPRi perturbation of enhancers and
430 promoter loci allowed us to functionally validate several components of the GRN, reinforcing their involvement
431 in cortical excitatory neurogenesis.
432

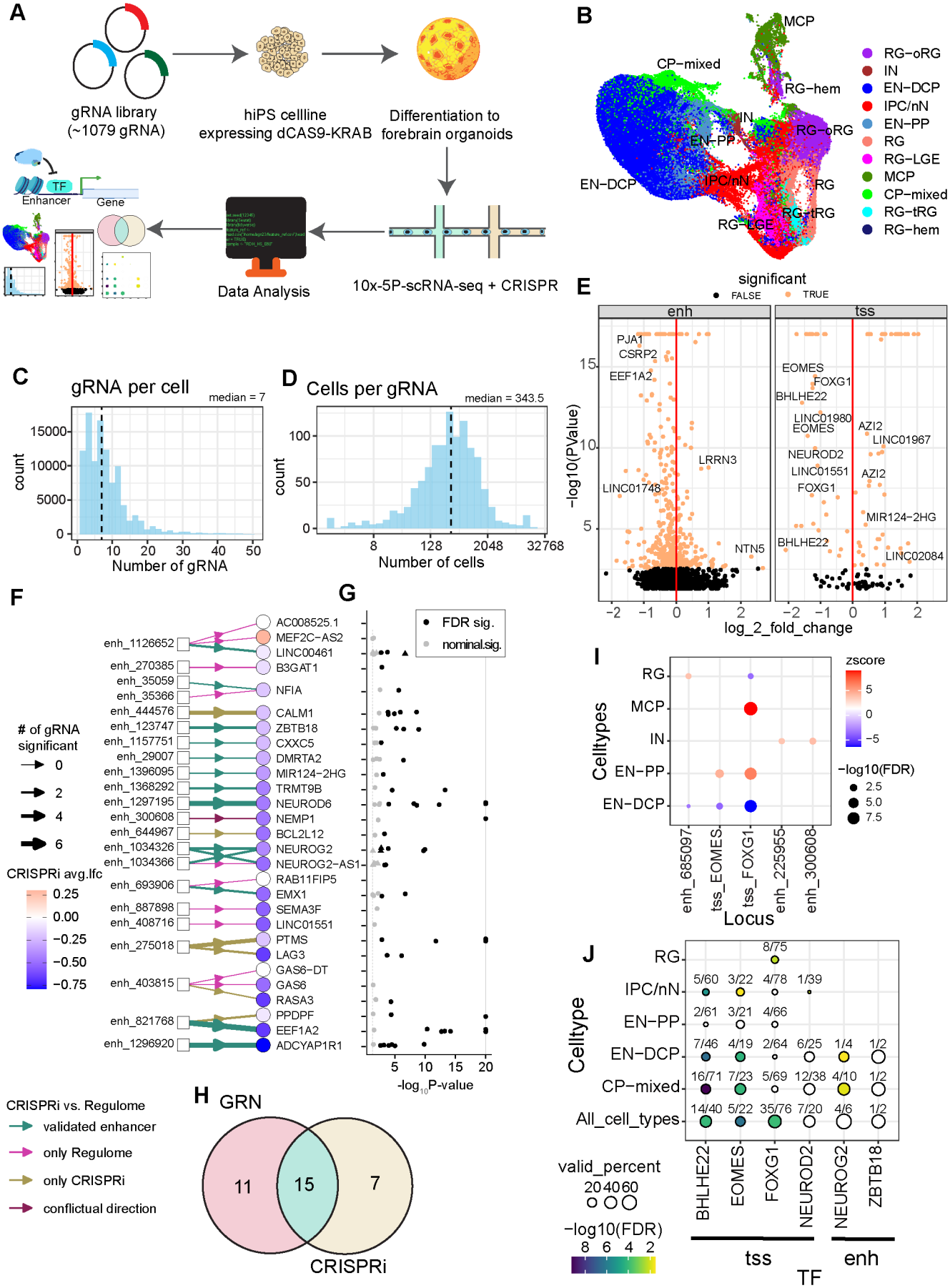
A
gRNA library
(~1079 gRNA)
hiPS cellline
expressing dCAS9-KRAB
Differentiation to
forebrain organoids
10x-5P-scRNA-seq + CRISPR
Data Analysis
Enhancer
Gene
TF
B
MCP
CP−mixed
RG−hem
IN
RG−oRG
EN−PP
EN−DCP
IPC/nN
RG
RG−LGE
RG−tRG
RG−oRG
IN
EN−DCP
IPC/nN
EN−PP
RG
RG−LGE
MCP
CP−mixed
RG−tRG
RG−hem
C
gRNA per cell
median = 7
count
Number of gRNA
D
Cells per gRNA
median = 343.5
count
Number of cells
E
significant
FALSE
TRUE
enh
tss
PJA1
CSRP2
EEF1A2
LRRN3
LINC01748
NTN5
EOMES
FOXG1
BHLHE22
LINC01980
EOMES
AZI2
LINC01967
NEUROD2
LINC01551
AZI2
FOXG1
MIR124−2HG
BHLHE22
LINC02084
−log10(PValue)
log_2_fold_change
F
# of gRNA
significant
0
2
4
6
CRISPRi avg.lfc
0.25
0.00
−0.25
−0.50
−0.75
enh_1126652
enh_270385
enh_35059
enh_35366
enh_444576
enh_123747
enh_1157751
enh_29007
enh_1396095
enh_1368292
enh_1297195
enh_300608
enh_644967
enh_1034326
enh_1034366
enh_693906
enh_887898
enh_408716
enh_275018
enh_403815
enh_821768
enh_1296920
AC008525.1
MEF2C−AS2
LINC00461
B3GAT1
NFIA
CALM1
ZBTB18
CXXC5
DMRTA2
MIR124−2HG
TRMT9B
NEUROD6
NEMP1
BCL2L12
NEUROG2
NEUROG2−AS1
RAB11FIP5
EMX1
SEMA3F
LINC01551
PTMS
LAG3
GAS6−DT
GAS6
RASA3
PPDPF
EEF1A2
ADCYAP1R1
G
FDR sig.
nominal.sig.
-log10 P-value
CRISPRi vs. Regulome
validated enhancer
only Regulome
only CRISPRi
conflictual direction
H
GRN
11
15
7
CRISPRi
I
zscore
5
0
−5
−log10(FDR)
2.5
5.0
7.5
Celltypes
RG
MCP
IN
EN−PP
EN−DCP
enh_685097
tss_EOMES
tss_FOXG1
enh_225955
enh_300608
Locus
J
Celltype
RG
IPC/nN
EN−PP
EN−DCP
CP−mixed
All_cell_types
8/75
5/60 3/22 4/78 1/39
2/61 3/21 4/66
7/46 4/19 2/64 6/25 1/4 1/2
16/71 7/23 5/69 12/38 4/10 1/2
14/40 5/22 35/76 7/20 4/6 1/2
valid_percent
20 40 60
−log10(FDR)
8 6 4 2
BHLHE22
EOMES
FOXG1
NEUROD2
NEUROG2
ZBTB18
tss
enh
TF

435 **Figure 5. CRISPRi validation of GRN enhancers. See also Figure S9.**

436 **A.** Workflow representing enhancer validation by a pooled CRISPRi approach.

437 **B.** UMAP at TD30 annotated by cell types as in Fig.2C.

438 **C-D.** Histogram showing distribution of the number of gRNAs per cell (C) and cells per gRNA (D) at TD30.

439 **E.** Volcano plots displaying gene expression change in gRNA-expressing versus non-expressing cells for genes
440 located in ±1MB region centered on the targeted locus; gRNAs are separated by promoter-gRNA (tss) and
441 enhancer gRNA (enh). Orange = significant differential expression with FDR < 0.1.

442 **F.** Regulatory graph comparing enhancer-gene links (boxes-to-circles arrows) identified by CRISPRi to links
443 identified in the GRN (arrow color, with "validated" (green) when significant in both experiments). Circle
444 color=CRISPRi-averaged log2-fold change, arrow thickness show number of significant gRNA.

445 **G.** Dot plot shows p-value for each gRNA perturbing the corresponding gene expression (black = FDR <0.1).

446 **H.** Venn Diagram showing intersection of GLE-gene links predicted by GRN and links called by CRISPRi
447 experiment. Intersection corresponds to 46.8% of total links tested. Link with conflicting result was added in
448 both sets for representation.

449 **I.** Significant change in cell fate due to perturbation of promoter (tss) or enhancer (enh_ID#, see **table S1** for
450 precise region). color= z-score compared to overall distribution; dot size = significance (FDR-corrected z-test)
451 (**Methods**).

452 **J.** Validation rate of predicted downstream targets of TF after gRNA mediated silencing of TF's expression (dot
453 size = percent of GRN-targets validated with number of genes indicated (validated / tested), color= Fisher exact-
454 test FDR corrected significance for enrichment of GRN-targets in CRISPRi results).
455

5. FOXG1 loss of function validated the gene regulatory network

FOXG1 was identified as one of the top candidate drivers of the ASD phenotypes in the GRN, so we did an exhaustive analysis of its central influence on the development of forebrain organoids. *FOXG1* upstream regulatory network comprised 14 activating GLEs in its *cis*-regulatory region (chr14:28,751,330–30,3825,86), which are bound by 11 repressors (including the top 3 TFs with increased activity in normoASD, FOXB1, LMX1B, and FOXA1) and 2 activators (NFIL3, ZEB1) with additional other indirect putative regulators upstream (**Fig. 6A**). In scRNA-seq data, *FOXG1* was strongly expressed in forebrain RG cells, silenced in hem-RG, preplate (EN-PP) and medial cortical plate (MCP), and re-expressed in postmitotic EN-DCP and IN of the dorsal cortical plate (DCP) (**Fig. 6B**). Consistent with this, we found that several TFs that repressed *FOXG1* (such as EBF3, FOXB1, FOXA1, ZNF823 and LMX1B, **Fig. 6A**) activated EN-PP genes and/or repressed EN-DCP genes (**Fig. 2E**). Downstream binding targets of FOXG1 included 418 activated GLEs and 281 repressed GLEs across the genome, suggesting that FOXG1 could act as an activator or as a repressor of enhancer activity (**Fig. S10A, Table S2**). Through those enhancers, we identified 111 downstream genes in the regulon of FOXG1, including 8 TFs (*POU3F3, BCL11A, LHX2, MEIS2, MEOX1, OTX2, SOX13, ZNF503*, **Fig. S10B**, **Fig. S3**). FOXG1 activated targets were expressed in RG progenitor, IN (e.g., *MEIS2*) and EN-DCP (e.g., *BCL11A, LHX2*), while some of its repressed targets (e.g., *OTX2*) were expressed in cells with medial fates (hem-RG, and MCP cells) (**Fig. 6B, Fig. S10C**). Finally, inside the GRN, FOXG1 competes preferentially with FOXB1, LMX1B or POU5F1B and collaborates more specifically with FOXK2, POU3F3 or FOXO3 across shared targets (**Fig. S10D**).

Several targets of FOXG1 were validated by CRISPRi (**Fig. 5J**). To further validate the regulon of FOXG1 in a focused experiment, we generated iPSC lines with FOXG1 loss of function mutations (FOXG1-/). CRISPR/Cas9 genome editing was used to introduce frame-shifting indels (see **Methods**), resulting in generation of a premature stop codon and a truncated FOXG1 protein lacking the forkhead-DNA binding domain (**Fig. 6C**). We then assessed differences in gene expression in organoids by bulk RNA-seq at TD30/60 by comparing two homozygous FOXG1-/- edited lines to two FOXG1+/+ control lines (termed LOF-DEGs, **Table S4,T3, Methods**). LOF-DEGs comprised 250 downregulated genes and 620 upregulated genes (**Fig. 6D**). The top downregulated LOF-DEG was *FOXG1* itself, suggesting that the FOXG1 exerts a positive autoregulatory effect on its expression or that the *FOXG1* truncated mRNA undergoes non-sense mediated decay. We observed that genes expressed in EN-DCP and RG were downregulated in LOF-DEG, while gene expressed in EN-PP, RG-hem and MCP, such as OTX2, were upregulated (**Fig. 6D,E**). This was concordant with the results of the CRISPRi-mediated *FOXG1* downregulation which showed that cells with gRNA targeting the *FOXG1* promoter exhibited a fate shift towards MCP and EN-PP (**Fig. 5I** and **S9I**). We also noted that cell cycle genes were overall downregulated (GO:0007049, p-value = 4.5×10^{-11} in FOG1 LOF downDEG, including genes such as MKI67 or TOP2A; **Table S4,T3**), which is consistent with microcephaly phenotypes resulting from FOXG1 LOF in humans[37,38].

When comparing the FOXG1 LOF-DEGs to the GRN, 37% of the 111 FOXG1 targets predicted by the GRN (30 repressed and 11 activated) were significant LOF-DEGs with concordant direction of change (**Fig. 6F**). FOXG1 activated targets in the GRN were enriched in genes downregulated in FOXG1-loss-of-function (Fisher's exact test p-value = 1.5×10^{-6}) whereas FOXG1 repressed targets in the GRN were enriched in genes upregulated in FOXG1 LOF (p-value= 2.1×10^{-13}) (**Fig. S10E**). For the remaining 70 FOXG1 targets in the GRN the direction of change in FOXG1 LOF-DEG remained concordant with the GRN prediction in a majority of cases (FDR > 0.05). Out of 41 gene targets validated by the LOF approach, 20 targets were also validated by CRISPRi, including *ERBB4, OTX2, POU3F3, MEIS2, SOX13* and *ID3* (**Fig. 6F**). Next, the LOF-DEG results were used as an input for TF activity perturbation analysis, which yielded FOXG1 as one of the strongest drivers of the LOF-DEGs with predicted decrease in activity (**Fig. 6G**), confirming our approach for identifying driver TFs from differential expressions using the GRN (**Fig S6**). Thus overall, the FOXG1 LOF experiment validated the constructed GRN. Finally, we observed that gene expression alterations induced by the FOXG1 LOF experiment were negatively correlated with macroASD pDEGs and positively correlated with normoASD pDEGs (**Fig. 6H**). This was attributable to top upregulated genes in macroASD being downregulated in LOF-DEGs, and to upregulated genes in normoASD being upregulated in LOF-DEGs. This similarity between ASD

506 pDEGs and FOXG1 LOF-DEGs supported the hypothesis that a FOXG1 dysregulation in opposite directions
507 drives a strong part of the ASD phenotype in each cohort.

508 Altogether, this is consistent with the role of FOXG1 in repressing medial fates in mammalian forebrain
509 development [39,40], where its inactivation leads to a decrease of dorsal cortical fates and an increase in medial
510 fates. Put together, the forebrain organoid system confirmed and reproduced the fundamental role of FOXG1
511 during development.

512
513

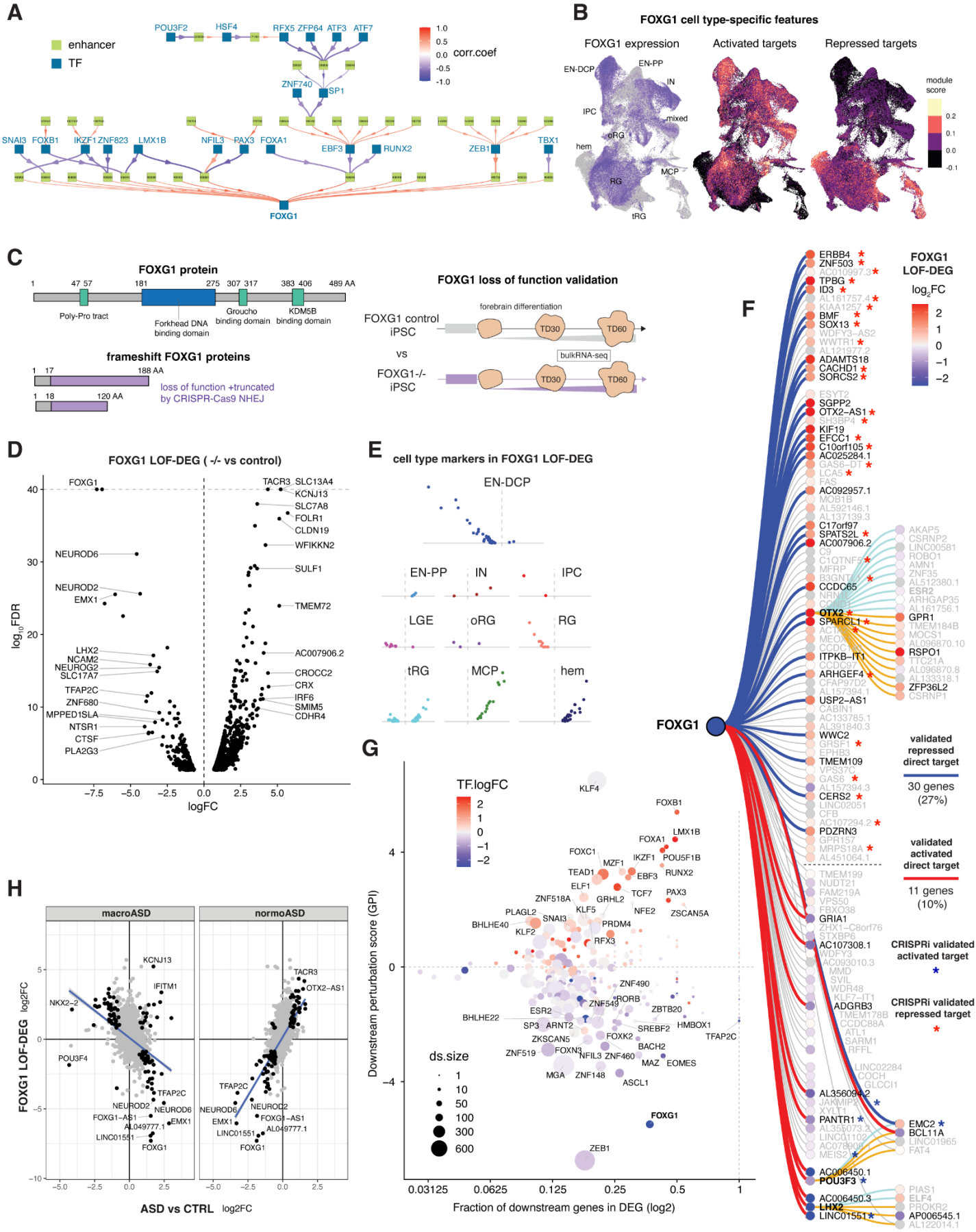
A
enhancer
TF
corr.coef
POU3F2
HSF4
RFX5
ZFP64
ATF3
ATF7
ZNF740
SP1
SNAI3
FOXB1
IKZF1
ZNF823
LMX1B
NFIL3
PAX3
FOXA1
EBF3
RUNX2
ZEB1
TBX1
FOXG1
B
FOXG1 cell type-specific features
FOXG1 expression
Activated targets
Repressed targets
module score
EN-DCP
EN-PP
IN
IPC
mixed
oRG
hem
MCP
RG
tRG
C
FOXG1 protein
Poly-Pro tract
Forkhead DNA binding domain
Groucho binding domain
KDM5B binding domain
frameshift FOXG1 proteins
loss of function +truncated by CRISPR-Cas9 NHEJ
FOXG1 loss of function validation
forebrain differentiation
FOXG1 control iPSC
vs
FOXG1-/- iPSC
TD30
TD60
bulkRNA-seq
D
FOXG1 LOF-DEG (-/- vs control)
log10FDR
logFC
E
cell type markers in FOXG1 LOF-DEG
EN-DCP
EN-PP
IN
IPC
LGE
oRG
RG
tRG
MCP
hem
F
FOXG1 LOF-DEG
log2FC
FOXG1
validated repressed direct target
30 genes (27%)
validated activated direct target
11 genes (10%)
CRISPRi validated activated target
CRISPRi validated repressed target
G
TF.logFC
ds.size
Downstream perturbation score (GPI)
Fraction of downstream genes in DEG (log2)
H
macroASD
normoASD
FOXG1 LOF-DEG log2FC
ASD vs CTRL log2FC

516 **Figure 6: Validating the downstream targets of the master regulator FOXG1 by CRISPR loss of function.**

517 **A.** Upstream regulators of FOXG1 including their respective cis-GLE and upstream TFs.

518 **B.** UMAP plots showing FOXG1 expression level in cell types juxtaposed with the positive module score
519 expression of its downstream activated and repressed target genes.

520 **C.** CRISPR-induced FOXG1 loss of function experiment. Schematic representation of the normal FOXG1
521 protein and the two predicted out-of-frame truncated proteins generated by CRISPR/Cas9 cleavage and non-
522 homologous end joining (NHEJ), retaining only 17-18 amino acids (AA) of the normal FOXG1 protein and
523 depleted of all the FOXG1-functional domains, including the forkhead DNA-binding domain.

524 **D.** Volcano plot of FOXG1 LOF-DEGs (comparing FOXG1 LOF vs non-edited and the founder iPSC line).

525 **E.** Volcano plots as in **d** highlighting FOXG1 LOF-DEGs that have cell type-specific expression, highlighting
526 the strong downregulation of EN-DCP genes and upregulation of medial fate (Hem, MCP).

527 **F.** Graph of FOXG1 regulon with targets colored by FOXG1 LOF-DEG results. Edges connecting FOXG1 to
528 its targets are colored in blue for repression or red for activation when validated by FOXG1 LOF-DEG. Fisher's
529 exact test confirmed that both FOXG1 activated targets are enriched in genes downregulated during FOXG1-
530 loss-of-function (p-value = 1.5×10^{-6}) and FOXG1 repressed targets are enriched in genes upregulated during
531 FOXG1 loss-of-function (p-value= 2.1×10^{-13}). Direct target genes are organized from top to bottom or bottom
532 to top based on their original correlation level with FOXG1 in the GRN. Asterisks indicate targets validated by
533 CRISPRi at FOXG1 promoter (see **Fig. 5J**); note they are among the strongest correlated genes. Secondary
534 targets of FOXG1 are also reported (through OTX2, POU3F3 or LHX2 regulation).

535 **G.** Perturbation plot for FOXG1 LOF-DEG, plotting for each TF in the GRN, the fraction of its regulon in LOF-
536 DEGs (x-axis) versus its activity perturbation score (as in **Fig. S6A**). Log-2 fold change of the TF itself (color)
537 and its regulon size (dot size) are indicated. Note that this analysis uses the GRN and the FOXG1 LOF-DEG
538 result to *naively* re-identify FOXG1 as one of the main drivers of the difference.

539 **H.** Confusion plots comparing logFC results between FOXG1 LOF-DEG and ASD vs Ctrl pDEG for macroASD
540 and normoASD. Top genes by distance from the origin are shown. Linear regression line is shown in blue
541 (Pearson's correlation R=-0.4 and 0.63, respectively, with both p-val $< 2.2.10^{-16}$)
542
543

Discussion

Using parallel epigenomic and transcriptomic datasets we constructed a regulome encompassing gene and enhancers in developing organoids. We leveraged the identification of proximal and distal gene-enhancer relationships and TFBS to infer regulatory action of TF on both enhancer activity and linked gene expression. The obtained network captured the driving forces behind time transitions and cell type specification during neurogenesis. Experimental validation via CRISPRi and FOXG1-LOF analyses strengthened the biological relevance of the network and highlighted specific TF cascades, notably implicating FOXG1, BHLHE22, and EOMES in the regulation of excitatory neuron specification in ASD.

By using iPSCs derived from idiopathic ASD individuals we identified the TFs and dysregulated enhancers that drive the imbalance of excitatory neurons previously discovered in this ASD cohort [15]. Specifically, we suggest that a dysregulation of FOXG1, BHLHE22 and EOMES expression in opposite directions in ASD with macrocephaly and ASD with normocephaly drives the excitatory neuron imbalance in opposite directions in these ASD subtypes. Dysregulated genes in the FOXG1 LOF experiment were largely overlapping with those affected in macroASD and normoASD, strongly suggesting that FOXG1 is a central causal factor of differential gene expression in ASD. While based on a limited number of individuals, our study is a first draft of gene regulatory interactions disrupted in this disorder during early neural development.

A limitation of existing GRNs is the reliance on correlation analyses to define regulatory links. In our case we limited the use of correlation and used it to supplement primary signals such as noisy predictions of TFBS, although we acknowledge that TF transcript levels are not always predictive of TF activity. Yet, GRN demonstrates considerable predictive power as evidenced by the CRISPRi and FOXG1 LOF validations, the moderate validation rate for enhancer-gene links suggests that additional layers of regulatory control such as chromatin conformation changes, combinatorial TF binding, and context-dependent enhancer activity are not fully captured by our current model. Interestingly, while the great majority of enhancers were activators of gene expression, negative correlations between TF levels and enhancer activity were just as abundant as positive one, suggesting that ~50% of developmental TF could act as repressors and confirming the notion that repression is essential for establishing precise patterns of gene expression during development [41]. Future GRN could incorporate proteomic information to account for post-transcriptional and post-translational modifications as important determinants of TF activity. While we could delineate from our GRN major collaborators and competitors of each TF (**Fig. S4**), further data collection would also help refine non-linear combinatorial effects occurring when multiple TFs co-regulate the same enhancers and genes. Another limitation of our GRN approach was the reliance on bulk-level data. This precluded a clear understanding of whether observed links in the GRN were specific to a given cell type or shared across cells. Nonetheless, we intersected the GRN with our own as well as external scRNAseq and scATAC data (**Figs. 1I and 2C-G**) and have found supporting evidence from single-cell data. Specifically, when genes are expressed in a cell type, their linked enhancers were also active in the same cell type, and such phenomenon involved active enhancers more often than repressing enhancers (**Fig. 2C-G**). While we show that the network captured major cell type specification, other subpopulation-specific regulatory interactions can be further delineated by expanding sample collections, including later stages and larger cohorts of individuals, and by incorporating single-cell level information in building of the network. Indeed, scATAC-seq data that captures open chromatin regions in each cell type overlapped only in part with ChIP-seq data and our regulome showed limited overlap with a recently described scATAC-seq organoid regulome[14], suggesting that combining both histone marks and open chromatin data at single cell level could fully resolve the regulatory events occurring in each cell type.

Altogether, the regulome establishes a hierarchy between TFs and cognate enhancers that controls the dynamics of cell differentiation during typical and atypical human neurodevelopment. We show that fundamental TFs like FOXG1 can drive cascades that are extremely complex in humans, with hundreds of downstream enhancers and genes. Untangling the complexity of these regulatory interactions through regulatory network analysis may reveal the paths of convergence behind the genetic heterogeneity of human developmental disorders such as ASD, schizophrenia or intellectual disabilities.

593 **Resource availability**
594
595 All unpublished codes are described in the Methods section of the paper.
596 This study did not generate new unique reagents or DNA constructs.
597
598 Primary cell lines and iPSC lines are shared via the Infinity BiologiX LLC repository (https://ibx.bio/) or
599 available from the corresponding author after MTA.
600
601 Datasets reported in this study are available through the NIMH Data Archive (NDA). As specified in our
602 consent form, data are available under controlled access for patient's privacy.
603 The scRNA-seq and scATAC-seq data are under collections #C3957, url:
604 https://nda.nih.gov/edit_collection.html?id=3957 and collection #2821, url:
605 https://nda.nih.gov/edit_collection.html?id=2821
606 The bulk RNA-seq and bulk ChIP-seq data are under collection #C2424, url:
607 https://nda.nih.gov/edit_collection.html?id=2424.
608 Data will be accessible through study #2322, url: https://nda.nih.gov/study.html?id=2322

609
610 **Acknowledgments**
611
612 We are grateful to the families and children for their participation in this study. We thank Soraya Scuderi for
613 help with the ChIP-seq protocol. We acknowledge Elise M. Cummings, Gloria Han, and Kelly Powell for help
614 with subject recruitment and clinical characterization to produce iPSC lines and Arijit Panda for help with data
615 upload into NDA and sharing. We thank Guilin Wang and Christopher Castaldi, and the Yale Center for
616 Genome Analysis for library preparation, deep sequencing and Cell Ranger analysis. We thank Caihong Qiu
617 and Jason Thomson at the Yale Stem Cell Center for the generation of the iPSC lines. We acknowledge the
618 Yale Center for Clinical Investigation for clinical support in obtaining the biopsy specimens.
619
620 **Funding:**
621
622 National Institutes of Health grant R01 MH109648 (FMV)
623 Simons Foundation Awards No. 399558 and 632742 (FMV, AAbyzov)
624 National Institutes of Health grants UM1HG012053, R01MH125236, RM1HG011123 (GEC, CAG)
625 The Yale Stem Cell Center is supported in part by the Regenerative Medicine Research Fund.
626
627 **Author contributions:**
628
629 Conceptualization, design, supervision: FMV, AAbyzov
630 Patient recruitment and acquisition of clinical data: McP, KP, PV, KC, LT
631 Skin biopsies: ASzekely
632 Primary cell culture, reprogramming and iPSC QC: LT
633 Organoid generation and processing for multiomic assays: JM, AJ, AS, AAmiri
634 Bulk RNA-seq and ChIP seq bioinformatic analysis: FW, SN, AJ
635 scATAC-seq bioinformatic analyses: FW
636 Zim3-dCas9 construct generation: MPN, DMR, MEW
637 CRISPRi experiment: AN, AJ, BL, CAG, GEC
638 gRNA library cloning, lentivirus production: MPN
639 FOXG1-loss of function lines experiment: AJ
640 Secondary bioinformatic analyses: AJ, SN, AN, DC
641 Writing—original draft: AJ
642 Writing—review & editing: AJ, AN, JM, FW, DC, AAbyzov, FMV
643

644 **Competing interests:** Authors declare that they have no competing interests.

645

646 ## STAR METHODS

647 ### Lead contact

648 Further information and requests for resources and reagents should be directed to and will be fulfilled by the
649 lead contact, Flora M. Vaccarino (flora.vaccarino@yale.edu).

650 ### Human Subjects/Ethical statement

651 All iPSC lines used in this study were described in a previous report where subject recruitment, clinical
652 information and iPSC generation are fully described [15]. Human subjects were recruited through several research
653 projects at the Yale Child Study Center. Written informed consent was obtained from each participant enrolled
654 in the study, and all research was approved by the Yale University Institutional Review Board (HIC#
655 1104008337) and Yale Center for Clinical Investigation at Yale University and was performed in accordance
656 with the Declaration of Helsinki. Human participants' names and other HIPAA identifiers were removed from
657 all sections of the manuscript, including supplementary information. The participants agreed to data sharing of
658 genomic unidentified data using controlled data access. All methods were performed according to relevant
659 regulations and guidelines of Yale University, including the Biological Safety Committee and ESCRO
660 committee of Yale University.

661 ### Organoid preparation

662 All iPSC lines and forebrain organoids preparations used in this study were identical to a previous report (see
663 **Data S1**) [15]. Briefly, IPSC lines from controls and ASD-probands were propagated in parallel and grown in
664 mTeSR1 media (StemCell Technologies). Forebrain organoids were generated using dual SMAD inhibition
665 (SB431542, 10µM and LDN193189, 1µM, 7 days), followed by a proliferation phase (FGF2, 10 ng/ml + EGF,
666 10 ng/ml, 7days) and a terminal differentiation phase (starting at day 17, denominated TD0) in terminal
667 differentiation media composed of Neurobasal medium supplemented with 1% N2, 2% B27 w/o vitamin A, 15
668 mM HEPES, Glutamax, NEAA and 55 µM 2-ME, with 10 ng/ml BDNF (R&D), 10 ng/ml GDNF (R&D). See
669 [15] for full details.

670 ### Chromatin immunoprecipitation

671 Native ChIP was carried out as previously described [13]. For chromatin pull-down, the following antibodies were
672 used: anti-H3K4me3 (Cell Signaling, Cat#9751S), anti-H3K27ac (Active Motif, Cat# 39133), anti-H3K27me3
673 (Cell Signaling, cat# 9733S) and H3K4me1 (Diagenode, cat#C15410037). ChIP-libraries and sequencing were
674 performed at the Yale Center for Genome Analysis. Paired-end DNA sequencing (2x100bp) was performed on
675 an Illumina Hi Seq2000 to an average depth of 40M reads per sample. Organoids for ChIP-seq and bulk RNA-
676 seq were collected in parallel from the same batch of differentiation.

677 ### RNA extraction and sequencing

678 Organoids samples were collected at TD0, TD30 and TD60. Total RNA extraction was performed from at least
679 20 dissociated organoids per sample using Arcturus PicoPure RNA isolation kit (AppliedBiosystems, cat.
680 12204-01). Library preparation was performed with rRNA depletion and sequenced on an Illumina
681 Hiseq/Novaseq to obtain an average depth of 40M reads per sample (paired-end 100bp reads) at the YCGA.
682 Organoids for bulk RNA-seq and ChIP-seq were collected in parallel from the same batch of differentiation.

683 ### Generation of stable line expressing Zim3-dCas9

684 CRISPRi relies on the expression of a nuclease-deactivated dCas9 fused to a strong transcriptional repressor,
685 the KRAB (Krüppel-associated box) domain, which recruits endogenous factors that trimethylate histone H3 on
686 Lys9 (H3K9me3) to silence the activity of a region targeted by specific guide RNAs (gRNAs) [29,30]. The
687 PiggyBac transposase system was used to establish a line expressing Zim3-dCas9 for CRISPRi library
688 screening. Vector iF53 PB-Zim3-dCas9-mScarlet-Hygro (Addgene #204726) was obtained from Michael Ward

689 (NIH/NINDS) and used to transfect the control male iPSC line RDH913-03#9 (generated in house [42]). 0.8
690 million single-cell suspension was plated in 1 well of a 6 well plate coated with Matrigel and mTeSR plus was
691 supplemented with Y compound (5µM). After 4 hours of plating, cells were transfected by Lipofectamine Stem
692 Transfection Reagent (STEM00008, Thermo Fisher Scientific) with total of 3ug DNA plasmid cocktail of
693 transposase and transposon (molar ratio of 1:5). Cells were selected with 50 µg/mL hygromycin B (10687-010,
694 Invitrogen), and mScarlet expression was monitored to ensure dCas9 expression.

695 **gRNA selection and library cloning**

696 104 target loci were selected for the single-cell CRISPRi forebrain organoid validation experiment, which were
697 composed of 94 GLEs (selected from the full set of GLE in**Table S2**), and 10 promoters. The 94 GLEs, each
698 targeted with up to 10 gRNAs (median: 10 gRNAs/GLE; range: 6-10 gRNAs/GLE) consisted of two groups.
699 First, 17 GLEs centrally involved in the EN regulatory hub in the ADS subnetwork (**Fig 3**) were selected. To
700 ensure efficient targeting by 10 gRNAs, we trimmed each of the 17 GLEs (mean size: 9.6kb) to 2kb, by centering
701 the 2kb window around the midpoint of the 100bp subregion of the GLE that has the highest number of TF
702 binding sites as predicted by FIMO [43] using default setting and the HOCOMOVO v11 full human TF motif
703 database. Second, 77 GLEs were selected based on the criterion that they harbor a schizophrenia-associated tag
704 SNP (n=1249 SNPs, from Table S2 of Trubetskoy et al[44]. Similarly, because 38 of these 77 GLEs were longer
705 than 2kb, we trimmed them to the 2kb subregions centered around the SNP it harbors to ensure efficient
706 targeting. After selecting and trimming a subset of these 94 GLEs, we then evenly divided each target region to
707 10 bins to design one gRNA per bin, with guidescan2, requiring specificity score >0.2 and prioritized by
708 efficiency score when multiple gRNAs passed the filter. This resulted in up to 10 gRNAs per GLE (median: 10
709 gRNAs/GLE; range: 6-10 gRNAs/GLE). The 10 gene promoter targets also consisted of two groups. First, six
710 TFs involved in neuronal maturation or differentiation (BHLHE22, FOXG1, EOMES, NEUROD2, LHX6,
711 LXM1B) were targeted with 10 gRNAs each from Horlbeck et al.'s hCRISPRi-v2 library[32]. Among these, LHX6
712 has two promoters targeted by Horlbeck et al., so we selected the top 5 ranking gRNAs per promoter. Second,
713 four positive control genes (GRN, CDH2, TFRC, UBQLN2) were targeted with 3 gRNAs each from Horlbeck
714 et al.'s hCRISPRi-v2 library, which serve as technical controls to evaluate the efficacy of CRISPRi repression,
715 as they have been previously shown to be efficiently repressed by CRISPRi in iPSC-derived neurons [33]. Finally,
716 100 non-targeting gRNAs (9.3% of final library) were added as negative controls from a curated set from Yao
717 et al. [45]. In total, the final gRNA library consisted of 1079 gRNAs.

718 To clone the gRNAs into a lentivirus vector, we first constructed a lentiviral gRNA expression plasmid by
719 combining a U6-gRNA cassette containing the gRNA-(F+E)-combined scaffold sequence with an EGFP-P2A-
720 PAC cassette into a lentiviral expression backbone (modifier version of Addgene#83925) using Gibson
721 assembly. Next, we ordered the 1079-gRNA oligonucleotide library through Twist Bioscience in the following
722 sequence format:

723 ATATATCTT GTGGAAAGG ACGAAACAC CG[19/20-bpprotospacer]GT TTAAGAGCTA TGC TGG
724 AAACA GCATAG

725 And the library was cloned into the Esp3I-digested vector backbone by Gibson Assembly. The library was
726 sequencing-verified by Next Generation Sequencing.

727

728 **Lentiviral production**

729 7 million 293Ts were plated in the afternoon into 12 mL complete Opti-MEM* in a 10cm cell culture dish. The
730 next morning, Lipofectamine 3000 reagent was prepared with Opti-MEM and mixed well. A DNA mix of
731 psPAX2 (9.75ug), pMD2.G (3.25ug) and gRNA plasmid pool (4.3ug) was prepared in Opti-MEM followed by
732 the addition of P3000. Sample was vortexed briefly. The Lipofectamine 3000 mix and DNA mix were combined
733 1:1 and incubated for 15 minutes at room temperature. Half the media (6 mL) was removed from the dish before
734 adding 3 mL of L3000 / DNA mix dropwise. The cells were incubated for 6 hours before discarding media and
735 adding 12mls of complete Opti-MEM. The supernatant was collected 24 hours after transfection, stored at 4C,
736 and replaced with 12mls complete Opti-MEM. The supernatant was collected again, 48 hours after transfection

737 and pooled with the first harvest. The supernatant was passed through a 0.45um filter before adding 4x LentiX
738 concentrator. Filtered supernatant was stored overnight at 4C. The following morning, sample was spun down
739 at 1700g for 45 minutes, aspirated and resuspended in 1/50 of the original volume of complete Opti-MEM.

740

741 **CRISPRi library infection**

742 Four million cells of the RDH913-03#9 line stably expressing Zim3-dCas9 were transduced with the gRNA
743 library with MOI of 5. After 24h of infection, cells were allowed to grow in virus free media. Cells were then
744 selected with 1 µg/ml puromycin (GIBCO/Thermo Fisher Scientific; Cat. No. A1113803) for 6 days followed
745 by 1 week in drug free media to form colonies. The line was differentiated to forebrain organoids as described
746 previously.

747 **10x genomics scRNA-seq**

748 iPSC line infected with CRISPRi gRNA library, and organoids at TD0 and TD30 were harvested for scRNA-
749 seq. Single-cell suspension was prepared using Accutase. Cells were processed using 10× Genomics single-cell
750 library preparation protocol with 20,000 cells targeted per libraryusing a 10× Chromium high-throughput chip
751 (Next GEM X) and Chromium Next GEM Single Cell 5'V3 Reagent Kits with Feature Barcode technology for
752 CRISPR Screening (10× Genomics, Inc, Document number CG000418, Rev C). For correct cell recovery, one
753 library was collected at undifferentiated iPSC and TD0 stage and 6 libraries were collected at TD30 stage. Gene
754 expression libraries were sequenced at 500 M reads/library and gRNA amplified libraries at 50 M reads/library
755 on Illumina HiSeq.

756 **FOXG1 LOF line**

757 Loss-of-function (LOF) mutations in the FOXG1 gene were obtained by CRISPR-Cas9 genome editing as
758 previously described [46]. Briefly, a guide RNAs (gRNAs) targeting the beginning of the first and only exon of
759 the FOXG1 genes (5' CAGGCTGTTGATGCTGAACG3') followed by the PAM seq 5' AGG 3' was used to
760 generate FOXG1 LOF iPSC lines. Cas9/gRNA mediated indels were generated in a control iPSC male line
761 (1123-01#3) by non-homologous end joining (NHEJ), which resulted in frameshifts and premature stop codons,
762 thus generating FOXG1 truncated proteins and presumably FOXG1 LOF alleles. Single cell-derived edited
763 clonal lines, each containing a homozygous or heterozygous genetic mutation in the FOXG1 locus, were
764 generated from the 1123-01#3 iPSC edited line by the limiting dilution process and screened by Sanger
765 sequencing to identify and validate the FOXG1 mutation in each clone. Genomic DNA from single clones was
766 extracted, PCR was performed to amplify the targeted region, and the PCR products were analyzed by Sanger-
767 sequencing. Upon genotyping by Sanger-seq, one of the edited clones, was also analyzed by whole genome
768 sequencing at 30x sequencing coverage [46]. Two homozygous mutations generated in different iPSC clonal lines
769 were used in this work: the deletion of 10 base pairs (bps) or the insertion of 1 bp (**Fig. 6C**), both resulting in
770 frameshift and premature stop codon, generating a 188 or 120 amino acid-truncated protein, retaining only 17
771 or 18 amino acids (AA) of the normal FOXG1 protein, respectively. Both versions of the truncated FOXG1
772 protein are depleted of all the FOXG1-functional domains, including the forkhead DNA binding domain (see
773 schematic of the resulting FOXG1 truncated proteins in **Fig. 6C**). These FOXG1 -/- lines were compared to
774 control FOXG1 +/+ lines, including both the founder iPSC line before editing and clonal iPSC lines where the
775 CRISPR/Cas9-induced DNA breaks didn't result in detectable genome edits.

776

777 **BIOINFORMATIC AND STATISTICAL DATA ANALYSIS**

778 **Enhancer discovery**

779 ChIP-seq reads were mapped to the UCSC hg38 reference genome using bowtie2 [47]. ChromHMM version 1.22
780 [17] was used to segment the genome based on the ChIP-seq profile. ChromHMM fits an emission profile for each
781 experimental group, which we defined as organoid TD + donor ASD diagnosis. We manually determined that a
782 Hidden Markov Model with nine hidden states provides the best fit for the data, based on how many states
783 aligned with the roadmap epigenome emissions signature. These states were grouped into broad regulatory

784 categories: states: 1, 8, and 9 were defined as promoter states ("Prom"), 2 and 3 as repressed states ("Rep"), and
785 the remainder as enhancer states ("Enh") (**Fig. 1c**).

786 To construct a set of candidate regulatory regions that are consistent across all experimental conditions, we
787 adapted our previous strategy [13] to merge and filter H3K27Ac ChIP-seq peaks. MACS2 [48] was used to call
788 "original peaks" (OP) for each ChIP-seq sample against the corresponding DNA input collected during the ChIP
789 experiment. Peaks from different samples with at least 1 bp overlap were merged using bedtools to generate
790 H3K27Ac consensus peaks. Consensus peaks were then annotated based on unambiguous overlap with the
791 hidden states inferred by ChromHMM. Briefly, if at least 60% of positions in a consensus peak overlapped with
792 a particular broad category in a given stage, the consensus peak was annotated with that category at that stage;
793 otherwise, it was annotated as "Mix". Stagewise annotations were consolidated into a global annotation for each
794 consensus peak according to the following strategy: If the consensus peak was annotated as "Mix" in any stage,
795 its global annotation was also "Mix". Consensus peaks that were annotated as "Prom" in one stage and "Enh"
796 in another were also annotated as "Mix" globally. Otherwise, the global annotation took the most active
797 annotation from any one stage, i.e. "Prom" or "Enh". "Rep" was attributed a consensus annotation only if all
798 stages were annotated with "Rep". To increase confidence, we further required putative enhancers (i.e.
799 consensus peaks annotated as "Enh") to be supported by at least four samples, in other words, each
800 corresponding consensus peak was merged by OPs from at least four samples.

801 **Linking enhancers to genes and TF**

802 The process of assigning putative enhancers to genes involves two strategies as previously described [13]. Briefly,
803 transcription start sites (TSS) for all protein-coding and lncRNA genes were defined from GENCODE (v33) [49].
804 Enhancers within 21kb of any TSS on the linear genome were linked to the respective genes. These were
805 supplemented with high-confidence long-range interactions between enhancers and a 1kb region around the TSS
806 derived from Hi-C contact matrices in human fetal cortex [18] and hSC lines [19,20] with 10-kb resolution.
807 For transcription factor binding site analysis, homer2 [50] was used to test for enrichment of 1,201 human
808 transcription factor position weight matrices (PWMs) from JASPAR2020 [51] among the DNA sequence of the
809 GLEs. Transcription factor binding sites (TFBS) with an FDR-corrected enrichment p-value less than 0.01 were
810 considered significant.

811 **Bulk RNA-seq analysis and differential gene expression**

812 RNA-seq reads were aligned to the hg38 genome using STAR (v2.7) [52] and annotations from GENCODE (v33)
813 [49]. Gene-level counts were estimated using *featureCounts* function from Subread (v2)[53]. Sequencing batch
814 effects were removed using ComBat-seq [54]. Gene filtering (function *filterByExpr*), normalized RPKM
815 expression values and all described differential expressed gene tests (DEGs) were generated following edgeR
816 pipeline (v3.26)[55]. For the different DEGs presented in the study (results in **Data S4**), log-2 fold change (log2FC)
817 and FDR-corrected p-values were computed from filtered counts with the *glmFit/glmLRT* functions, with
818 "organoid stage" (TD0/30/60) and "family" used as covariates when appropriate (see **Data S1 for samples**
819 **metadata**).

820 **Differential enhancer activity**

821 Similar to RNA reads, H3K27ac read counts in all gene linked enhancers (173,400 GLEs) estimated using
822 featureCounts v2.0.3 [53] were considered a measure of enhancer activity and tested for differential activity using
823 edgeR (v3.4). For any given contrast between groups, enhancers with low activity were filtered out using the
824 *filterByExpr* function in R and differential activity was evaluated using *glmFit* and *glmLRT* functions in edgeR.

825 **Enhancer-gene regulatory network**

826 For each downstream gene target of a GLE, a pairwise Spearman correlation was computed between the GLE
827 activity (H3K27ac ChIP-seq counts normalized as RPKM using EdgeR) and the expression of the target gene
828 (RNA-seq RPKM). P-values were adjusted using the Benjamini-Hochberg method. Similarly, regulatory impact
829 of TF on each GLE presenting the cognate TFBS was estimated as the Spearman correlation between expression
830 of the TF transcript (RNA-seq RPKM) and the activity of the bound GLE (H3K27ac ChIP-seq RPKM). For
831 both GLE-to-gene and TF-to-GLE, putative regulatory relationships were retained if passing FDR < 0.01 and

absolute correlation coefficient > 0.25. The selected relationships were assembled into an *enhancer-gene regulatory network* (directed graph, available in **Data S2, T2-3**). Visualization and network-based computation were done using the R packages igraph (v1.4.3), tidygraph (v1.2.3) and ggraph (v2.1).

Synthetic TF-gene-regulatory network

The synthetic TF-to-gene regulatory network was built from the original enhancer-gene regulatory network so that TF are connected to genes through at least one identified enhancer element presenting the cognate TFBS. First, cases where both the TF-GLE and the GLE-gene edges existed (so both having significant correlations) were retained to link each TF to each of its downstream genes (see **Fig. S2** for the number of cases of regulatory cascades considered and retained). Then, Spearman's correlation between the TF and its downstream gene(s) expressions (both RNA RPKM) were calculated and retained if FDR < 0.01 and absolute correlation coefficient (r > 0.25 or r < -0.25). Edges were then retained if the sign of the TF-to-gene correlation was coherent with the TF-to-GLE and GLE-to-gene correlation signs, which is equivalent to:

$$\rho_{\text{TF-gene}} \cdot \rho_{\text{TF-GLE}} \cdot \rho_{\text{GLE-gene}} > 0$$

For plotting, the correlation between the genes was used to compute a positive edge weight in the final gene regulatory network with weight = $r_{\text{TF-gene}}/2 + 0.5$ (or its inverse depending on the algorithm weight definition). Networks plotted in the different figures were obtained using either Sugiyama layout, which limits the number of edge crossing in the final hierarchical plot or Kamada-Kawai layout in igraph/ggraph, which effectively repulse strongly in the final plot genes connected by a negative correlation edge (repressive) than genes connected by a positive correlation.

TF prioritization by TF perturbation score

For integrating gene regulatory network with results obtained from differential gene expression results (DEG, by edgeR), we were inspired by the *AUCell GRN* method for scRNA-seq data (part of the SCENIC suite [56]) which evaluates the activity of the TF based on the downstream targets expression enrichment in each cells. To infer similar effect using bulk data and DEG results, we used an adaptation of the *geometric perturbation index* [57]. We exemplified the use of this **TF perturbation score** in **Fig. S6a-b**. For a TF with N targets in the GRN, its perturbation score for a given DEG result was defined as:

$$TF.score = \frac{1}{\sqrt{N}} \sum_{i=1}^{N} \rho_{GRN.TF \to i} \times log_2 FC_{DEG.i} \ (1 - FDR_{DEG.i})$$

where for the ith target, $r_{\text{GRN.TF->i}}$ is the Spearman's correlation coefficient between the TF and the ith target expression level across samples as described above (corresponding to the edge's weight in our GRN, with: -1 < r < 1). The DEG's log_2FC value of the downstream gene is weighted by its false non-discovery rate ($1\text{-}FDR_{DEG}$) to downplay the effect of genes with low significant change without having to set a threshold on the significance. For each edge, the product of the sign of the logFC (-1 for DOWNregulation and +1 for UPregulation) with the sign of the correlation coefficient (+1 for activation, -1 for repression) effectively evaluate if the direction of change is compatible with the action of the TF without having to treat separately activation/repression and upregulation/downregulation (see **Fig. S6b** for examples). This generates a score with biological interpretation: a positive TF perturbation score indicates an upregulation of the TF actions described in the GRN (i.e. TF activating/repressing actions on its downstream genes), a near-zero score suggest little implication of the TF in the observed DEG results, and a negative score indicates a downregulation of the TF action. The score only considers the differential expression of the downstream targets and not of the TF itself and use the built GRN to infer the degree to which a change in the TF activity could have explained those observed differential expression.

This score was used in **Fig. 2B** with timeDEG (using in that case only activating edges with r >0 to compute the score to facilitate interpretation, see **Fig. S6C** showing all result); **Fig. 2E** with celltype-DEG (see below); **Fig. 3B** with macro-ASD DEG; **Fig. 3D** with normo-DEG; and **Fig. 6G** with FOXG1 loss of function DEG. For plots, we compared the TF perturbation score with the differential expression of the TF itself (dot blue-red color gradient), the number of target N (dot size) and the fraction of those downstream targets that meet strict DEG criteria (regardless of direction of change, cutoff: FDR < 0.05 or 0.01 and absolute log_2FC > 0.25). Note that using the square root of N stems from the original geometrical definition of the metric and has here for effect to

give higher score to genes with larger number of targets. For the specific case of **Fig. 2e**, we applied the TF perturbation score using cell type-specific DEGs computed in our scRNA-seq dataset. For cell type-specific DEGs (**Data S5**), the logFC and BH-adjuster p value were computed in Seurat (v3) using the *FindMarkers* function which performs differential expression test by comparing cells from each cell type to the remaining cells using a Wilcoxon's rank sum test.

Intersection of enhancers regions external datasets

Overlap of enhancer consensus peaks identified in our data with gene enhancer external datasets were evaluated using BedTools (*intersectBed*) [58]. From this present study we used 3 different level: the full 367,587 consensus peaks annotated as "active enhancer" in any of our sample group ("all enhancers"), the 173,347 gene-linked enhancer subset (GLE, following the gene linkage step, **Data S2,T1**) and the 42,035 GLEs that show significant correlation with any linked gene or with any TF with TFBS as described above, **Data S2,T2-3**) For Screen enhancer regions from the ENCODE project [22], "candidate enhancer" coordinates in hg38 was downloaded from https://screen.wenglab.org/ (v3). For Genehancer dataset [23], the GeneHancer_v5.14 was obtained through the Genecard website. Enhancer dataset from Amiri et al. previously generated from fetal brain, iPSCs and organoids at TD0, TD11,TD30 by our lab was also used [13].

Intersection with ATAC-seq/scATAC-seq external datasets were performed using BedTools [58] considering a minimum of 20% overlap between the length of our enhancers and the length of peaks from the external dataset. For **Fig. 1**, the resulting data was plotted using the 'UpSetR' package in R [59].

Intersection with Single cell ATAC-seq peak from parallel organoid data

To validate the enhancer activity in single cells, we intersected our list of enhancers with peaks called from 29 scATACseq samples using BedTools [58] (**Data S5**, T2). To process scATACseq data, Cell Ranger ATAC 2.0.0 [60] along with pre-built reference arc-GRCh38-2020-A-2.0.0 was applied to each sample from calling cells to generating a peak-cell count matrix. Signac vignette (https://stuartlab.org/signac/articles/pbmc_vignette.html) [61] was followed to filter the count matrix of each sample with the following cut-offs: cells containing at least 200 features, features present in at least 10 cells, log10 of fragments in peak regions per cell within two standard deviation of the mean, nucleosome signals between 2 and 4, TSS enrichment greater than 2, reads in peaks over 15% and less than 5% of peaks overlapping with black list. scATACseq data were annotated using label transfer method implemented in Seurat [62] along with our previously annotated scRNAseq datasets as reference [15]. Next peaks per library or per cell type were called using MACS2 as recommended by Seurat developers.

TF interactome

TF-TF interactome graph based on shared gene targets between TFs in the GRN (**Data S3**). Specificity of the overlap was assessed by a connection specificity index (CSI) which is independent of the direction of the TF action (i.e. repress/activate) but evaluates if the overlap in regulon is higher for that pair of TF than with all other TFs (CSI) [63]. Collaboration vs competition was assessed by the Pearson's correlation coefficient (Inter.cor) between the TF's weights across all gene targets (negative values indicate opposite actions on the downstream genes on average).

scCRISPRi data analysis

CRISPRi gene expression and gRNAs libraries were processed with Cellranger (version 9.010X Genomics) A threshold of 5 gRNA UMIs/cell (--min-crispr-umi) was used to assign gRNAs per cell during Cellranger count function. For the TD30 dataset, all libraries were aggregated before proceeding with data analysis. Cellranger files were further processed with Seurat (V 5.0.1) for filtering low quality cells, data normalization, and UMAP projection. To test genes susceptible to be affected by each gRNA in *cis*, chromosome position for all gRNAs in hg38 version were extracted using *BSgenome* package (v1.70.2) and genes located in a 1Mb upstream and downstream window around each gRNA were fetched using *getBM*() function of *biomaRt* package (v2.58.2). Distal genes linked to enhancers beyond 1Mb regions previously identified from HiC data were added to the list of tested genes for each loci. Pairing of gRNAs and unique hgnc symbols was carried out and these pairs were subjected to 'SCEPTRE' tool analysis [35]. Counts matrices for genes and gRNA were extracted from Seurat object and used to construct a single-cell covariate matrix with non-zero expression in gRNA and gene

expression libraries. These data sets were exported using packages, sceptre (v0.10.2) and ondisc(v1.2.0) for processing with 'NextFlow' based sceptre pipeline. sceptre pipeline was run with 'high' moi parameter, using positive control pairs as gRNA targeting the TSS of genes. Discovery pairs were selected based on genes falling in 1Mb window of respective gRNA. NTCs were tested against all genes from discovery pairs and calibration was performed. Multiple testing correction using Benjamini-Hochberg method was carried out to adjust the p-values and adj_p_value <0.1 was considered as significant. Change in cell fate was calculated by assessing percent alteration in each cell type for gRNAs obtained from sceptre analysis (p_value <0.05). Then mean percent alteration was calculated for each locus in all cell types. zscore was computed as following

$$zscore = \frac{\{x - mean(avg_{percent})\}}{sd(avg_{percent})}$$

Further, p-value was calculated using a two-tailed z-test and adjusted with BH correction.

Seurat *FindMarkers*() function using Wilcoxon's rank sum test was used to identify genome-wide DEGs for gRNAs targeting the TSS of a TF or for gRNAs targeting an enhancer with significant downregulation of a TF expression (after SCEPTRE analysis). All gRNAs targeting particular loci were combined into one group and background cells (without carrying gRNA targeting TSS of any TF) were used as control. FDR <0.05 was considered as significant alteration of gene expression.

References

1. Mariani, J., Simonini, M.V., Palejev, D., Tomasini, L., Coppola, G., Szekely, A.M., Horvath, T.L., and Vaccarino, F.M. (2012). Modeling human cortical development in vitro using induced pluripotent stem cells. Proc Natl Acad Sci U S A *109*, 12770-12775. 10.1073/pnas.1202944109.
2. Lancaster, M.A., Renner, M., Martin, C.A., Wenzel, D., Bicknell, L.S., Hurles, M.E., Homfray, T., Penninger, J.M., Jackson, A.P., and Knoblich, J.A. (2013). Cerebral organoids model human brain development and microcephaly. Nature *501*, 373-379. 10.1038/nature12517.
3. Pasca, S.P. (2018). The rise of three-dimensional human brain cultures. Nature *553*, 437-445. 10.1038/nature25032.
4. Visel, A., Taher, L., Girgis, H., May, D., Golonzhka, O., Hoch, R.V., McKinsey, G.L., Pattabiraman, K., Silberberg, S.N., Blow, M.J., et al. (2013). A high-resolution enhancer atlas of the developing telencephalon. Cell *152*, 895-908. 10.1016/j.cell.2012.12.041.
5. Thurman, R.E., Rynes, E., Humbert, R., Vierstra, J., Maurano, M.T., Haugen, E., Sheffield, N.C., Stergachis, A.B., Wang, H., Vernot, B., et al. (2012). The accessible chromatin landscape of the human genome. Nature *489*, 75-82. 10.1038/nature11232.
6. Gasperini, M., Tome, J.M., and Shendure, J. (2020). Towards a comprehensive catalogue of validated and target-linked human enhancers. Nat Rev Genet *21*, 292-310. 10.1038/s41576-019-0209-0.
7. Panigrahi, A., and O'Malley, B.W. (2021). Mechanisms of enhancer action: the known and the unknown. Genome Biol *22*, 108. 10.1186/s13059-021-02322-1.
8. Andersson, R., Gebhard, C., Miguel-Escalada, I., Hoof, I., Bornholdt, J., Boyd, M., Chen, Y., Zhao, X., Schmidl, C., Suzuki, T., et al. (2014). An atlas of active enhancers across human cell types and tissues. Nature *507*, 455-461. 10.1038/nature12787.
9. Boix, C.A., James, B.T., Park, Y.P., Meuleman, W., and Kellis, M. (2021). Regulatory genomic circuitry of human disease loci by integrative epigenomics. Nature *590*, 300-307. 10.1038/s41586-020-03145-z.
10. Markenscoff-Papadimitriou, E., Whalen, S., Przytycki, P., Thomas, R., Binyameen, F., Nowakowski, T.J., Kriegstein, A.R., Sanders, S.J., State, M.W., Pollard, K.S., and Rubenstein, J.L. (2020). A Chromatin Accessibility Atlas of the Developing Human Telencephalon. Cell *182*, 754-769 e718. 10.1016/j.cell.2020.06.002.
11. Song, M., Pebworth, M.P., Yang, X., Abnousi, A., Fan, C., Wen, J., Rosen, J.D., Choudhary, M.N.K., Cui, X., Jones, I.R., et al. (2020). Cell-type-specific 3D epigenomes in the developing human cortex. Nature *587*, 644-649. 10.1038/s41586-020-2825-4.
12. Nott, A., Holtman, I.R., Coufal, N.G., Schlachetzki, J.C.M., Yu, M., Hu, R., Han, C.Z., Pena, M., Xiao, J., Wu, Y., et al. (2019). Brain cell type-specific enhancer-promoter interactome maps and disease-risk association. Science *366*, 1134-1139. 10.1126/science.aay0793.
13. Amiri, A., Coppola, G., Scuderi, S., Wu, F., Roychowdhury, T., Liu, F., Pochareddy, S., Shin, Y., Safi, A., Song, L., et al. (2018). Transcriptome and epigenome landscape of human cortical development modeled in organoids. Science *362*. 10.1126/science.aat6720.
14. Fleck, J.S., Jansen, S.M.J., Wollny, D., Zenk, F., Seimiya, M., Jain, A., Okamoto, R., Santel, M., He, Z., Camp, J.G., and Treutlein, B. (2023). Inferring and perturbing cell fate regulomes in human brain organoids. Nature *621*, 365-372. 10.1038/s41586-022-05279-8.
15. Jourdon, A., Wu, F., Mariani, J., Capauto, D., Norton, S., Tomasini, L., Amiri, A., Suvakov, M., Schreiner, J.D., Jang, Y., et al. (2023). Modeling idiopathic autism in forebrain organoids reveals an imbalance of excitatory cortical neuron subtypes during early neurogenesis. Nat Neurosci *26*, 1505-1515. 10.1038/s41593-023-01399-0.
16. Roche, A.F., Mukherjee, D., Guo, S.M., and Moore, W.M. (1987). Head circumference reference data: birth to 18 years. Pediatrics *79*, 706-712.
17. Ernst, J., and Kellis, M. (2012). ChromHMM: automating chromatin-state discovery and characterization. Nat Methods *9*, 215-216. 10.1038/nmeth.1906.

994 18. Won, H., de la Torre-Ubieta, L., Stein, J.L., Parikshak, N.N., Huang, J., Opland, C.K., Gandal, M.J.,
995 Sutton, G.J., Hormozdiari, F., Lu, D., et al. (2016). Chromosome conformation elucidates regulatory
996 relationships in developing human brain. Nature *538*, 523-527. 10.1038/nature19847.
997 19. Jin, F., Li, Y., Dixon, J.R., Selvaraj, S., Ye, Z., Lee, A.Y., Yen, C.A., Schmitt, A.D., Espinoza, C.A.,
998 and Ren, B. (2013). A high-resolution map of the three-dimensional chromatin interactome in human
999 cells. Nature *503*, 290-294. 10.1038/nature12644.
1000 20. Rao, S.S., Huntley, M.H., Durand, N.C., Stamenova, E.K., Bochkov, I.D., Robinson, J.T., Sanborn,
1001 A.L., Machol, I., Omer, A.D., Lander, E.S., and Aiden, E.L. (2014). A 3D map of the human genome
1002 at kilobase resolution reveals principles of chromatin looping. Cell *159*, 1665-1680.
1003 10.1016/j.cell.2014.11.021.
1004 21. Li, L.M., and Arnosti, D.N. (2011). Long- and short-range transcriptional repressors induce distinct
1005 chromatin states on repressed genes. Curr Biol *21*, 406-412. 10.1016/j.cub.2011.01.054.
1006 22. Consortium, E.P., Moore, J.E., Purcaro, M.J., Pratt, H.E., Epstein, C.B., Shoresh, N., Adrian, J., Kawli,
1007 T., Davis, C.A., Dobin, A., et al. (2020). Expanded encyclopaedias of DNA elements in the human and
1008 mouse genomes. Nature *583*, 699-710. 10.1038/s41586-020-2493-4.
1009 23. Fishilevich, S., Nudel, R., Rappaport, N., Hadar, R., Plaschkes, I., Iny Stein, T., Rosen, N., Kohn, A.,
1010 Twik, M., Safran, M., et al. (2017). GeneHancer: genome-wide integration of enhancers and target
1011 genes in GeneCards. Database (Oxford) *2017*. 10.1093/database/bax028.
1012 24. Ziffra, R.S., Kim, C.N., Ross, J.M., Wilfert, A., Turner, T.N., Haeussler, M., Casella, A.M., Przytycki,
1013 P.F., Keough, K.C., Shin, D., et al. (2021). Single-cell epigenomics reveals mechanisms of human
1014 cortical development. Nature *598*, 205-213. 10.1038/s41586-021-03209-8.
1015 25. Trevino, A.E., Sinnott-Armstrong, N., Andersen, J., Yoon, S.J., Huber, N., Pritchard, J.K., Chang,
1016 H.Y., Greenleaf, W.J., and Pasca, S.P. (2020). Chromatin accessibility dynamics in a model of human
1017 forebrain development. Science *367*. 10.1126/science.aay1645.
1018 26. Ardhanareeswaran, K., Mariani, J., Coppola, G., Abyzov, A., and Vaccarino, F.M. (2017). Human
1019 induced pluripotent stem cells for modelling neurodevelopmental disorders. Nature reviews.
1020 Neurology *13*, 265-278. 10.1038/nrneurol.2017.45.
1021 27. Runge, K., Mathieu, R., Bugeon, S., Lafi, S., Beurrier, C., Sahu, S., Schaller, F., Loubat, A., Herault,
1022 L., Gaillard, S., et al. (2021). Disruption of NEUROD2 causes a neurodevelopmental syndrome with
1023 autistic features via cell-autonomous defects in forebrain glutamatergic neurons. Mol Psychiatry.
1024 10.1038/s41380-021-01179-x.
1025 28. Joshi, P.S., Molyneaux, B.J., Feng, L., Xie, X., Macklis, J.D., and Gan, L. (2008). Bhlhb5 regulates the
1026 postmitotic acquisition of area identities in layers II-V of the developing neocortex. Neuron *60*, 258-
1027 272. 10.1016/j.neuron.2008.08.006.
1028 29. Klann, T.S., Crawford, G.E., Reddy, T.E., and Gersbach, C.A. (2018). Screening Regulatory Element
1029 Function with CRISPR/Cas9-based Epigenome Editing. Methods Mol Biol *1767*, 447-480.
1030 10.1007/978-1-4939-7774-1_25.
1031 30. Klann, T.S., Black, J.B., Chellappan, M., Safi, A., Song, L., Hilton, I.B., Crawford, G.E., Reddy, T.E.,
1032 and Gersbach, C.A. (2017). CRISPR-Cas9 epigenome editing enables high-throughput screening for
1033 functional regulatory elements in the human genome. Nat Biotechnol *35*, 561-568. 10.1038/nbt.3853.
1034 31. Schmidt, H., Zhang, M., Chakarov, D., Bansal, V., Mourelatos, H., Sanchez-Rivera, F.J., Lowe, S.W.,
1035 Ventura, A., Leslie, C.S., and Pritykin, Y. (2025). Genome-wide CRISPR guide RNA design and
1036 specificity analysis with GuideScan2. Genome Biol *26*, 41. 10.1186/s13059-025-03488-8.
1037 32. Horlbeck, M.A., Gilbert, L.A., Villalta, J.E., Adamson, B., Pak, R.A., Chen, Y., Fields, A.P., Park,
1038 C.Y., Corn, J.E., Kampmann, M., and Weissman, J.S. (2016). Compact and highly active next-
1039 generation libraries for CRISPR-mediated gene repression and activation. eLife *5*.
1040 10.7554/eLife.19760.
1041 33. Tian, R., Gachechiladze, M.A., Ludwig, C.H., Laurie, M.T., Hong, J.Y., Nathaniel, D., Prabhu, A.V.,
1042 Fernandopulle, M.S., Patel, R., Abshari, M., et al. (2019). CRISPR Interference-Based Platform for
1043 Multimodal Genetic Screens in Human iPSC-Derived Neurons. Neuron *104*, 239-255 e212.
1044 10.1016/j.neuron.2019.07.014.

1045 34. Gasperini, M., Hill, A.J., McFaline-Figueroa, J.L., Martin, B., Kim, S., Zhang, M.D., Jackson, D.,
1046 Leith, A., Schreiber, J., Noble, W.S., et al. (2019). A Genome-wide Framework for Mapping Gene
1047 Regulation via Cellular Genetic Screens. Cell *176*, 377-390 e319. 10.1016/j.cell.2018.11.029.
1048 35. Barry, T., Wang, X., Morris, J.A., Roeder, K., and Katsevich, E. (2021). SCEPTRE improves
1049 calibration and sensitivity in single-cell CRISPR screen analysis. Genome Biol *22*, 344.
1050 10.1186/s13059-021-02545-2.
1051 36. Pinto, L., Mader, M.T., Irmler, M., Gentilini, M., Santoni, F., Drechsel, D., Blum, R., Stahl, R.,
1052 Bulfone, A., Malatesta, P., et al. (2008). Prospective isolation of functionally distinct radial glial
1053 subtypes--lineage and transcriptome analysis. Mol Cell Neurosci *38*, 15-42. S1044-7431(08)00026-2
1054 [pii]10.1016/j.mcn.2008.01.012.
1055 37. Takagi, M., Sasaki, G., Mitsui, T., Honda, M., Tanaka, Y., and Hasegawa, T. (2013). A 2.0 Mb
1056 microdeletion in proximal chromosome 14q12, involving regulatory elements of FOXG1, with the
1057 coding region of FOXG1 being unaffected, results in severe developmental delay, microcephaly, and
1058 hypoplasia of the corpus callosum. European journal of medical genetics *56*, 526-528.
1059 10.1016/j.ejmg.2013.05.012.
1060 38. Hettige, N.C., and Ernst, C. (2019). FOXG1 Dose in Brain Development. Front Pediatr *7*, 482.
1061 10.3389/fped.2019.00482.
1062 39. Muzio, L., and Mallamaci, A. (2005). Foxg1 confines Cajal-Retzius neuronogenesis and hippocampal
1063 morphogenesis to the dorsomedial pallium. J Neurosci *25*, 4435-4441. 10.1523/JNEUROSCI.4804-
1064 04.2005.
1065 40. Hanashima, C., Li, S.C., Shen, L., Lai, E., and Fishell, G. (2004). Foxg1 suppresses early cortical cell
1066 fate. Science *303*, 56-59. 10.1126/science.1090674.
1067 41. Gray, S., and Levine, M. (1996). Transcriptional repression in development. Curr Opin Cell Biol *8*,
1068 358-364. 10.1016/s0955-0674(96)80010-x.
1069 42. Scuderi, S., Kang, T.Y., Jourdon, A., Yang, L., Wu, F., Nelson, A., Anderson, G.M., Mariani, J.,
1070 Sarangi, V., Abyzov, A., et al. (2024). Specification of human regional brain lineages using orthogonal
1071 gradients of WNT and SHH in organoids. bioRxiv. 10.1101/2024.05.18.594828.
1072 43. Grant, C.E., Bailey, T.L., and Noble, W.S. (2011). FIMO: scanning for occurrences of a given motif.
1073 Bioinformatics *27*, 1017-1018. 10.1093/bioinformatics/btr064.
1074 44. Trubetskoy, V., Pardinas, A.F., Qi, T., Panagiotaropoulou, G., Awasthi, S., Bigdeli, T.B., Bryois, J.,
1075 Chen, C.Y., Dennison, C.A., Hall, L.S., et al. (2022). Mapping genomic loci implicates genes and
1076 synaptic biology in schizophrenia. Nature *604*, 502-508. 10.1038/s41586-022-04434-5.
1077 45. Yao, D., Tycko, J., Oh, J.W., Bounds, L.R., Gosai, S.J., Lataniotis, L., Mackay-Smith, A., Doughty,
1078 B.R., Gabdank, I., Schmidt, H., et al. (2024). Multicenter integrated analysis of noncoding CRISPRi
1079 screens. Nat Methods *21*, 723-734. 10.1038/s41592-024-02216-7.
1080 46. Panda, A., Suvakov, M., Mariani, J., Drucker, K.L., Park, Y., Jang, Y., Kollmeyer, T.M., Sarkar, G.,
1081 Bae, T., Kim, J.J., et al. (2023). Clonally Selected Lines After CRISPR-Cas Editing Are Not Isogenic.
1082 CRISPR J *6*, 176-182. 10.1089/crispr.2022.0050.
1083 47. Langmead, B., and Salzberg, S.L. (2012). Fast gapped-read alignment with Bowtie 2. Nat Methods *9*,
1084 357-359. 10.1038/nmeth.1923.
1085 48. Zhang, Y., Liu, T., Meyer, C.A., Eeckhoute, J., Johnson, D.S., Bernstein, B.E., Nusbaum, C., Myers,
1086 R.M., Brown, M., Li, W., and Liu, X.S. (2008). Model-based analysis of ChIP-Seq (MACS). Genome
1087 Biol *9*, R137. 10.1186/gb-2008-9-9-r137.
1088 49. Frankish, A., Diekhans, M., Ferreira, A.M., Johnson, R., Jungreis, I., Loveland, J., Mudge, J.M., Sisu,
1089 C., Wright, J., Armstrong, J., et al. (2019). GENCODE reference annotation for the human and mouse
1090 genomes. Nucleic Acids Res *47*, D766-D773. 10.1093/nar/gky955.
1091 50. Heinz, S., Benner, C., Spann, N., Bertolino, E., Lin, Y.C., Laslo, P., Cheng, J.X., Murre, C., Singh, H.,
1092 and Glass, C.K. (2010). Simple combinations of lineage-determining transcription factors prime cis-
1093 regulatory elements required for macrophage and B cell identities. Mol Cell *38*, 576-589.
1094 10.1016/j.molcel.2010.05.004.
1095 51. Fornes, O., Castro-Mondragon, J.A., Khan, A., van der Lee, R., Zhang, X., Richmond, P.A., Modi,
1096 B.P., Correard, S., Gheorghe, M., Baranasic, D., et al. (2020). JASPAR 2020: update of the open-

1097 access database of transcription factor binding profiles. Nucleic Acids Res *48*, D87-D92.
1098 10.1093/nar/gkz1001.
1099 52. Dobin, A., Davis, C.A., Schlesinger, F., Drenkow, J., Zaleski, C., Jha, S., Batut, P., Chaisson, M., and
1100 Gingeras, T.R. (2013). STAR: ultrafast universal RNA-seq aligner. Bioinformatics *29*, 15-21.
1101 10.1093/bioinformatics/bts635.
1102 53. Liao, Y., Smyth, G.K., and Shi, W. (2014). featureCounts: an efficient general purpose program for
1103 assigning sequence reads to genomic features. Bioinformatics *30*, 923-930.
1104 10.1093/bioinformatics/btt656.
1105 54. Zhang, Y., Parmigiani, G., and Johnson, W.E. (2020). ComBat-seq: batch effect adjustment for RNA-
1106 seq count data. NAR Genom Bioinform *2*, lqaa078. 10.1093/nargab/lqaa078.
1107 55. Robinson, M.D., McCarthy, D.J., and Smyth, G.K. (2010). edgeR: a Bioconductor package for
1108 differential expression analysis of digital gene expression data. Bioinformatics *26*, 139-140.
1109 10.1093/bioinformatics/btp616.
1110 56. Aibar, S., Gonzalez-Blas, C.B., Moerman, T., Huynh-Thu, V.A., Imrichova, H., Hulselmans, G.,
1111 Rambow, F., Marine, J.C., Geurts, P., Aerts, J., et al. (2017). SCENIC: single-cell regulatory network
1112 inference and clustering. Nat Methods *14*, 1083-1086. 10.1038/nmeth.4463.
1113 57. Martin, F., Thomson, T.M., Sewer, A., Drubin, D.A., Mathis, C., Weisensee, D., Pratt, D., Hoeng, J.,
1114 and Peitsch, M.C. (2012). Assessment of network perturbation amplitudes by applying high-
1115 throughput data to causal biological networks. BMC Syst Biol *6*, 54. 10.1186/1752-0509-6-54.
1116 58. Quinlan, A.R., and Hall, I.M. (2010). BEDTools: a flexible suite of utilities for comparing genomic
1117 features. Bioinformatics *26*, 841-842. 10.1093/bioinformatics/btq033.
1118 59. Conway, J.R., Lex, A., and Gehlenborg, N. (2017). UpSetR: an R package for the visualization of
1119 intersecting sets and their properties. Bioinformatics *33*, 2938-2940. 10.1093/bioinformatics/btx364.
1120 60. Satpathy, A.T., Granja, J.M., Yost, K.E., Qi, Y., Meschi, F., McDermott, G.P., Olsen, B.N., Mumbach,
1121 M.R., Pierce, S.E., Corces, M.R., et al. (2019). Massively parallel single-cell chromatin landscapes of
1122 human immune cell development and intratumoral T cell exhaustion. Nat Biotechnol *37*, 925-936.
1123 10.1038/s41587-019-0206-z.
1124 61. Stuart, T., Srivastava, A., Madad, S., Lareau, C.A., and Satija, R. (2021). Single-cell chromatin state
1125 analysis with Signac. Nat Methods *18*, 1333-1341. 10.1038/s41592-021-01282-5.
1126 62. Hao, Y., Hao, S., Andersen-Nissen, E., Mauck, W.M., 3rd, Zheng, S., Butler, A., Lee, M.J., Wilk, A.J.,
1127 Darby, C., Zager, M., et al. (2021). Integrated analysis of multimodal single-cell data. Cell *184*, 3573-
1128 3587 e3529. 10.1016/j.cell.2021.04.048.
1129 63. Fuxman Bass, J.I., Diallo, A., Nelson, J., Soto, J.M., Myers, C.L., and Walhout, A.J. (2013). Using
1130 networks to measure similarity between genes: association index selection. Nat Methods *10*, 1169-
1131 1176. 10.1038/nmeth.2728.
1132